CASL-U-2012-0163-000

Power uprates
and plant life extension

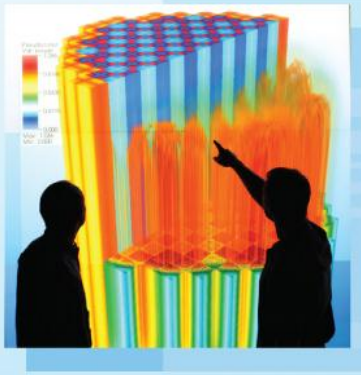

Engineering design
and analysis

Science-enabling
high performance
computing

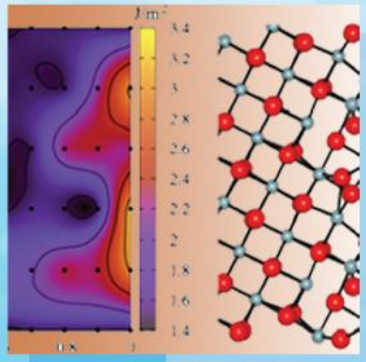

Fundamental science

Plant operational data

Consortium for Advanced Simulation of LWRs

L3:THM.CFD.P5.03

Mark Christon
LANL

Completed: 10/03/2012

U.S. DEPARTMENT OF ENERGY | Nuclear Energy

Sensitivity, Verification, and Validation Studies of STAR-CD, STAR-CCM+, and Nphase CFD Boiling Models

Isaac M. Asher[*], Timothy J. Drzewiecki[†], Timothy P. Grunloh[‡], Victor E. Petrov[§], Krzysztof J. Fidkowski[¶], Annalisa Manera[‖]

September 29, 2012

CASL Milestone L3-THM-CFD-P5-03

[*]Graduate Student, Department of Aerospace Engineering, University of Michigan
[†]Graduate Student, Department of Nuclear Engineering and Radiological Sciences, University of Michigan
[‡]Graduate Student, Department of Nuclear Engineering and Radiological Sciences, University of Michigan
[§]Research Scientist, Department of Nuclear Engineering and Radiological Sciences, University of Michigan
[¶]Assistant Professor, Department of Aerospace Engineering, University of Michigan
[‖]Associate Professor, Department of Nuclear Engineering and Radiological Sciences, University of Michigan

Executive Summary

This report documents the completion of milestone L3-THM-CFD-P5-03. The report is divided into two parts, one on sensitivity studies and one on validation.

The sensitivity study work contained herein extends the studies documented in two previous milestones, MNM.TH.Y1-2.05 and L3-THM-CFD-P3-01. MNM.TH.Y1-2.05 introduced simulations of the DEBORA test case using Star-CD and provided sensitivities to wall boiling model parameters for the model implemented in Star-CD. In milestone L3-THM-CFD-P3-01, we extended the sensitivity study to include additional parameters governing phase-to-phase heat and momentum transfer and parameters from the turbulence model. We also augmented the list of outputs, including the radial distribution of void fraction through a centroid measurement, and we provided grid convergence studies. The present milestone extends this work in the following ways:

1. We focus on an additional code: Nphase-CMFD
2. We outline the steps necessary to run the DEBORA case using Nphase-CMFD
3. We provide physically-motivated input parameter ranges to aid in identifying the dominant sensitivities.

The sensitivity study using Nphase-CMFD remains as comprehensive as possible in the models tested, given the present unavailability of a boiling model in Nphase-CMFD. We describe a workaround for this using a coupling with Star-CD. The test problem remains the same, a simulation of the DEBORA-10 experiment of $R12$ flowing through a vertical pipe with a heated test section. The results for this problem lead to the following general conclusions:

- Nphase will require wall boiling models in order to faithfully simulate CASL-relevant applications.
- Star-CD and Nphase (driven by Star-CD heat partitioning) yield similar results for the DEBORA simulation.
- New input parameter ranges indicate large sensitivities to the turbulent dispersion coefficient, the bubble diameter, and the lift coefficient.

The second part of the report concerns validation of the boiling models implemented in STAR-CD and STAR-CCM+. The target test cases are DEBORA and PSBT. We reach several conclusions in this study:

- The cross-section averaged void fraction is systematically overestimated in the low void fraction range, and underestimated in the higher void fraction range.
- The S-gamma model improves the Kurul-Podowski modeling of the bubble size in these cases.
- In the high void fraction range the current S-gamma model has practically no effect with respect to the base model.
- The S-gamma model has a considerable effect on the axial void fraction distribution

This report provides data and discussions supporting these conclusions.

Part 1
Sensitivity studies of STAR and Nphase CFD boiling models for the DEBORA test case

1 Introduction

This report describes ongoing work to use the Nphase-CMFD code to simulate coolant flow in a nuclear reactor core, with particular focus on the CRUD problem. The overall goal of this work is to perform a sensitivity study of the multiphase fluid dynamics models in Nphase. First, we will describe the grid and model setup, which was complicated by several factors. Following this, we converged and verified the solution. Further work was done to choose relevant parameters and their ranges for the sensitivity study. This work extends the literature survey from previous milestones. Finally, the sensitivity study was performed and the results interpreted.

1.1 Motivation

The motivation for looking at sensitivities comes from the observation that most CFD boiling and multiphase models rely on correlations with empirically-determined parameters. These parameters offer flexibility when matching theory to experimental data, which are generally limited and available for only a handful of geometries and conditions. The parameters then become a liability when simulating novel designs or conditions, as errors due to mistuning are generally not quantified. Furthermore, different codes implement different (variations of) certain models, and hence restricting attention to only one code risks drawing conclusions that are lacking in generality.

Knowledge of sensitivities of CFD results to these tunable parameters can aid uncertainty quantification (UQ) studies by effectively reducing the dimension of the parameter space. That is, parameters that do not strongly affect outputs may not need to be considered in the UQ studies. In addition, when combined with estimates of parameter variability, as is done in this work, sensitivity information can guide model improvement by identifying key parameters and associated models to which outputs are most sensitive.

1.2 Approach

Numerous models exist for simulating multiphase flow, boiling, and turbulence. A comprehensive treatment of all possible formulations is beyond the scope of this work. Instead, we choose to focus on a subset of models that are relatively standard and representative of those used in thermalhydraulics applications. Specifically, we use the models implemented in two software packages: Star-CD from CD-Adapco and Nphase-CMFD from RPI. The boiling model is somewhat more contentious among codes, and in the case of Nphase it is not yet implemented. We therefore "hard-wire" data from the heat partitioning distribution obtained using Star-CD when using Nphase for sensitivity studies.

1.3 The DEBORA Test Problem

The test problem consists of a heated circular pipe with R12 flowing vertically through it. The geometry is shown in Figure 1. We note that the system pressure is 1.459 MPa. The outputs of interest for the CRUD problem are the same as in previous work: pressure drop over the pipe (Δp),

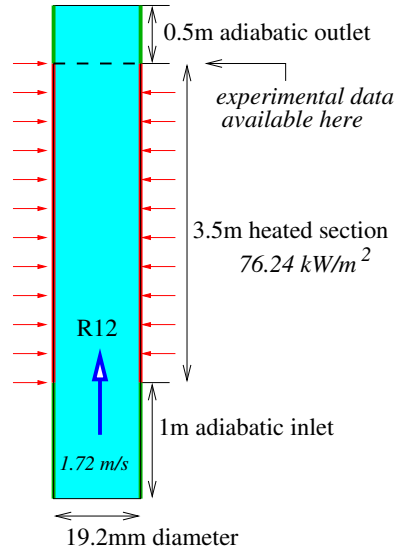

Figure 1: DEBORA problem setup. The cross-section is circular and simulations are performed using an axi-symmetric assumption.

average wall temperature ($\overline{T}_{\text{wall}}$), average void fraction at the measurement location ($\overline{\alpha}$), and radial centroid of the void fraction profile at the measurement location ($\overline{r}_{\alpha}$).

2 Simulation Codes

2.1 Star-CD

Star-CD employs an Eulerian multiphase model that is representative of treatments in other commercial codes. Boiling is modeled by a variation of the Kurul-Podowski heat-partitioning model. Star-CD serves as the baseline reference code for this work, and it provides heat-partitioning data to Nphase.

2.2 Nphase-CMFD

Developed at RPI, this finite volume, parallel code can handle two- and three-dimensional unstructured grids. Many built-in multiphase models are available, and user defined C-subroutines, with access to all data structures in the code, allow much flexibility. Currently, the following physical models are available

- High- and Low-Re $k - \epsilon$ turbulence models
- Level sets for interface tracking
- Pressure jump across phase interfaces
- Arbitrary number of phases/fields (e.g. bubble populations/regimes)
- Species and reaction terms for chemistry
- Bubble interaction and wall shear apportionment models

Some features that are necessary for the DEBORA case have not yet been implemented. First, there is no wall boiling model. Thus, one must provide some input specification of how the heat flux is partitioned among the liquid and vapor phases. Since this depends on the problem being solved, we used the heat partioning from the converged Star-CD solution.

Second, the bubble diameter is fixed for the entire domain. This could be overcome by defining multiple populations of bubbles, each with its own fixed size. However, that would require defining interactions between all of the bubble populations, which quickly becomes a very complex task. Instead, we simply specify a fixed bubble diameter based on the Star-CD solution.

Finally, there is no support for transferring solutions between meshes. This means that we must solve on our mesh of interest, starting from a programmable initial condition. A coarser mesh cannot be used to initialize the solution. This makes it more difficult to reach a converged solution and requires finding an initial condition with a stable path to the solution.

While investigating Nphase, it became necessary to document the major modeling differences between Nphase, Star-CD, and Star-CCM+ for later comparisons. The models used by each code can be compared side by side in a document prepared by the group, along with some information on other models developed by the multiphase community. This document also informs the choice of parameters and ranges in the sensitivity studies.

The following numerical controls are available in Nphase:

- 1st and 2nd order upwind and hybrid finite volume discretizations
- Coupled mass/momentum solve with algebraic multigrid acceleration
- Under-relaxation and pseudo time stepping
- Some robustness enhancements, e.g. limiting turbulent production
- Convergence based on state updates
- Restart capability

3 Problem Setup

3.1 Wall Boiling Model

Since wall boiling is not implemented, the user must set the heat partitioning programmatically in a C-subroutine. That is, the user decides, for every cell, the fraction of the wall heat flux that causes liquid heating and the fraction that causes bubble generation and the remaining that causes gas heating. In this example, as in the Star-CD heat partioning model, we set the gas heating to zero. That is, any heat that does not cause liquid heating will generate vapor. This can be a problem if the void fraction reaches 1.0, since then any excess heat that goes into gas generation is ignored and effectively lost. Thus, we must ensure that during the solution process, none of the cells near the heated wall have a void fraction of 1.0.

In order to have a realistic solution, we set the heat partitioning profile to the profile from the Star-CD DEBORA solution, which is shown in Figure 2. We took this approach because our overall goal is to calculate the model sensitivities in both Star-CD and Nphase, and to compare the codes. The profile taken from Star-CD was run on a uniformly spaced 800x20 mesh with residuals converged as documented in previous reports. The profile, which ranges from 0 to about 70% of

the heat going to gas generation, was fitted by hand with three quadratics. The resulting fit had an estimated L_2 error of 2.25 percentage points.

Gas generation in Nphase requires specifying a porous wall and injecting the gas with a small velocity. It precise velocity is not important, as long as it does not affect the overall momentum balance. The actual condition that is enforced is the imparted mass flux. The chosen velocity of 7.45×10^{-2} was verified to not significantly affect the momentum balance (contributes an additional 0.016% to the overall momentum at the wall).

3.2 Bubble Diameter

In the Nphase solution, the bubble diameter was fixed at 7×10^{-4}m. This value was chosen by visually inspecting the Star-CD solution. The converged temperature distribution was used to calculate the bubble diameter that Star-CD would have used (i.e. the $d(T)$ correlation), which gave $d \in [1.5 \times 10^{-4}, 18.46 \times 10^{-4}]$ with an average of 6.35×10^{-4}m. Thus, the fixed value gives a relatively good estimate of the average bubble diameter. The error was considered small compared to the large range of d in Star-CD. The sensitivity study will determine if this range of d has a significant influence on the solution and the outputs of interest.

3.3 Computational Mesh

The computational mesh to be solved on was a 2D, axisymmetric, structured mesh. Solutions were found using both the low-Re and high-Re turbulence models, which require different meshes. For the low-Re model, the mesh must resolve the entire viscous sublayer near the wall. For the DEBORA test case, this results in a very small grid spacing near the wall of 1.5×10^{-6}m which gives a y^+ slightly below 1 for the converged solution.

For the high-Re model, a much coarser mesh is possible, since we require the mesh spacing near the wall to have a $y^+ \gtrsim 50$. A spacing of 4×10^{-4} results in $50 \lesssim y^+ \lesssim 80$ for the converged solution. The mesh had 30 cells in the radial direction and 400 axially, which was deemed sufficient resolution by visual inspection. The only quantity that varies rapidly with respect to mesh spacing is the radial velocity, where there seems to be a discontinuity at the end of the heated section. In this work, we did not have time to investigate why this happens or if resolving this feature significantly changes the solution. However, we have encountered numerous cases in which the radial velocity distribution is strongly affected by parameters that otherwise have little or no effect on the solution. Thus, we assume that resolving the (relatively small) radial velocity is would not significantly change the solution. We should also note that the radial momentum equation almost always had the highest relative errors in converged solutions.

Although a solution on the low-Re mesh was converged, it was prohibitively expensive to do further tests or use it in the sensitivity study. Thus, all of the data and results in this report are based on the high-Re solution.

3.4 Additional Code

In order to reach a converged solution, an extra block of code was written to dynamically modify the false time step and relaxation factors. This was based on a simple strategy to accelerate the solution process if the solution is converging, and to severely slow down progress when the solution is degrading and becoming unstable. The only data available to identify how the solution is converging are the state updates (residuals of the governing equations are not computed). In

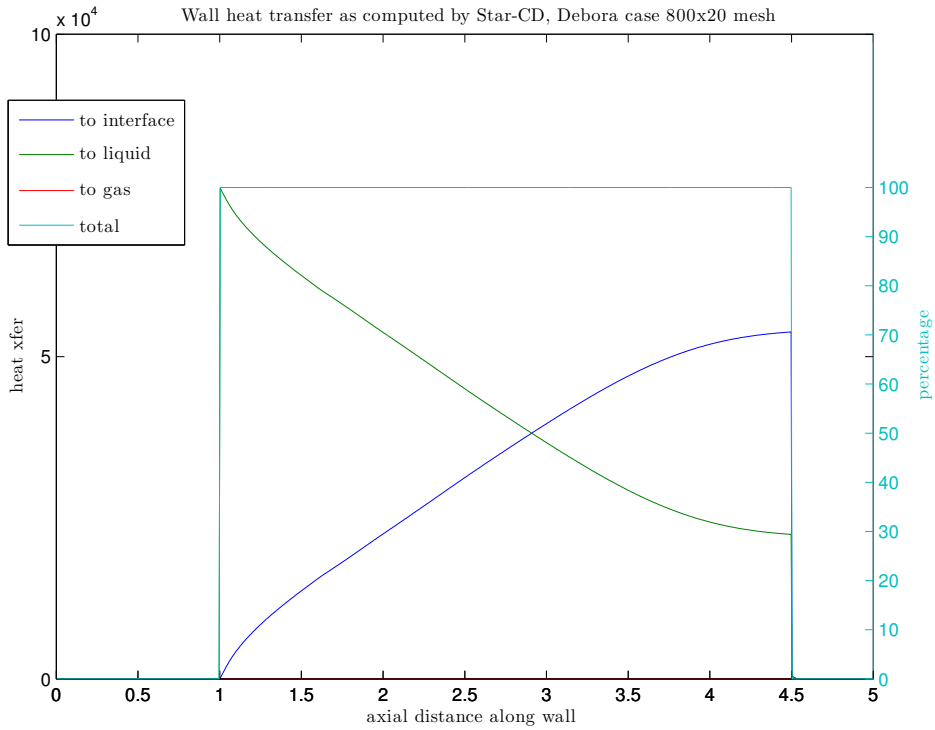

Figure 2: heat partitioning profile from Star-CD DEBORA solution.

addition, it would be advantageous to discard bad updates and re-calculate them with a smaller time step. This was possible only for some of the equations, since not all of the update values are available in the user-coded subroutines. In the end, the added capability contributed only modestly to the results.

The recommended method for assessing convergence in Nphase is checking the magnitude of the state updates, specifically the root-mean-squared update (not taking into account the mesh spacing). Since each variable is scaled differently (e.g. pressure is on the order of 10^6Pa, velocity around 1m/s), the updates must be compared to the magnitude of the state. To make this process easier, code was written to compute the root-mean-squared state, and convergence was assessed using the ratio RMS(update)/RMS(state). Note, the mesh spacing was not taken into account here. Also, rather than looking at each velocity component separately, we look for convergence of the magnitude of the velocity vector.

Another feature that was implemented was a ramping-up of the wall heat and mass fluxes during the initial phases of the solution, in order to automate the process of reaching a converged solution. As a result, it was necessary to add additional code to programmatically set the wall boundary condition and change it during iterations.

3.5 Getting to a Converged Solution

In order to arrive at a converged solution, we took a number of steps from simple flows to the final DEBORA case. At each stage, the solution from the previous stage was used as the initial condition. Before moving to the next stage, the solution at a given stage was converged as much as possible. The stages were

1. Compute the approximate, fully developed turbulent pipe flow solution using known profiles

from the literature. Velocity and pressure fields were computed.

2. Solve for the single-phase, unheated pipe flow. The goal is to solve for the turbulent quantities.

3. Solve for multi-phase, heated pipe flow with full heat flux but mass flux reduced to 10% of nominal.

4. Slowly increase to full mass flux.

4 Baseline Solution

The convergence of the DEBORA solution while increasing the mass flux is shown in Figure 3. The root-mean-square of the state update, normalized by the rms of the state, is plotted for the eight states. Each spike in the plot represents an increase in the mass flux and a restarting of the solution. The enthalpy ("h", the yellow line) converges quite quickly, since the energy equation is linear. The pressure and turbulent quantities ("p", "k", and "e") converge to the point where relative updates are $\approx 10^{-6}$. The void fraction and velocity magnitude ("a" and "u") do not converge as well, but relative updates are still less than 0.1%. Finally, the radial velocity component ("v", the green line) has constant oscillations around 1%. This may be due to the discontinuous nature of the radial velocity profile, as seen in Figure 4. Since the radial velocity component is not generally of much interest, and its magnitude is quite small compared to the axial velocity, we did not attempt to further address the issue.

The final solution is plotted in Figures 4 and 5. The calculation was done with an axisymmetric mesh, so only a cross section is shown. The top of the plot represents the wall of the cylinder, and the bottom is the centerline, and the flow is from left to right. The inlet effects, boundary layer, and radial velocity feature at the end of the heated section are apparent in Figure 4. Even though the velocity at the cell adjacent to the wall is far from zero, the wall functions in the High Re turbulence model enforce the correct boundary conditions. The heat transfer from the wall and the bubbles generated are apparent in Figure 5. The temperature reaches beyond the boiling point of 331.3K, so some bulk boiling occurs near the end of the heated section.

The void fraction is nearly constant close to the wall because the lift force is set to zero here. Further from the wall, the lift force causes the bubbles to migrate toward the center of the pipe. The baseline solution shown in Figure 5 uses a lift coefficient of $C_L = -0.03$ and the lift force is disabled within one bubble diameter from the wall ($\hat{y}_{\text{wall}} = 1$). The void fraction distribution is highly dependent on the chosen lift model and varies considerably between Nphase, Star-CD, and Star-CCM+. An experimentally determined void fraction profile is available at the end of the heated section, and Figure 6 shows this along with various computational models[1].

4.1 Checks and Verifications

The following checks were performed to ensure that the problem was set up correctly.

- Low- and High-Re models give similar solutions

- Verified energy conservation (modified due to gas injection)

[1]Note, the "step-ladder" effect for Star-CCM+ is merely an artifact of the sampling method chosen; it is not a part of the solution

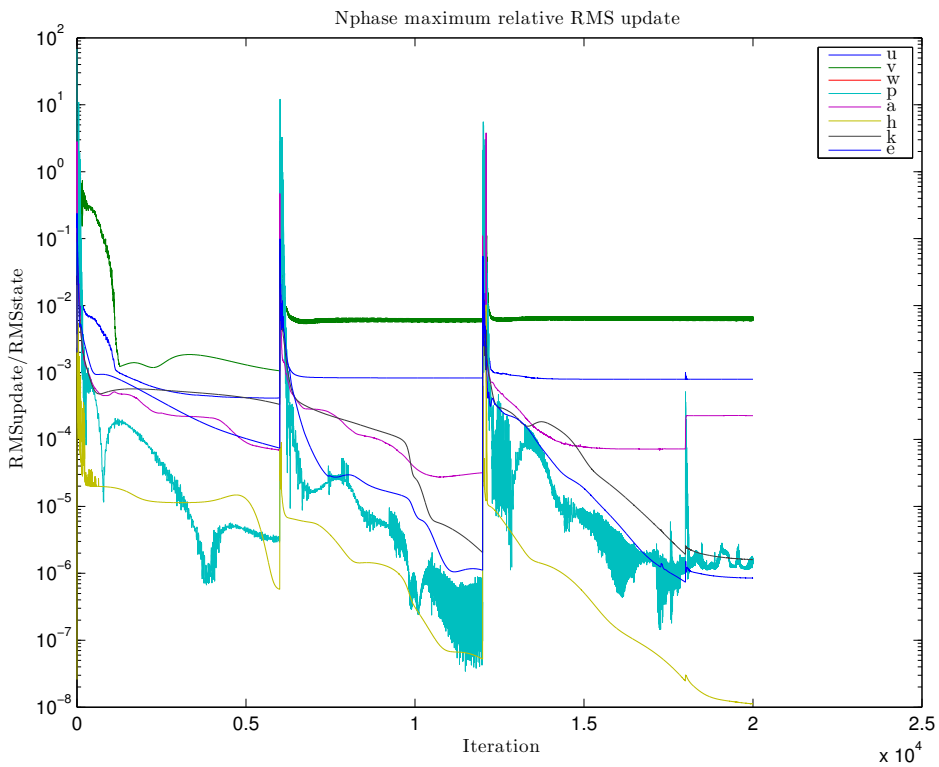

Figure 3: Convergence of Nphase baseline solution for DEBORA problem. Spikes are when mass flux was increased and solution process restarted.

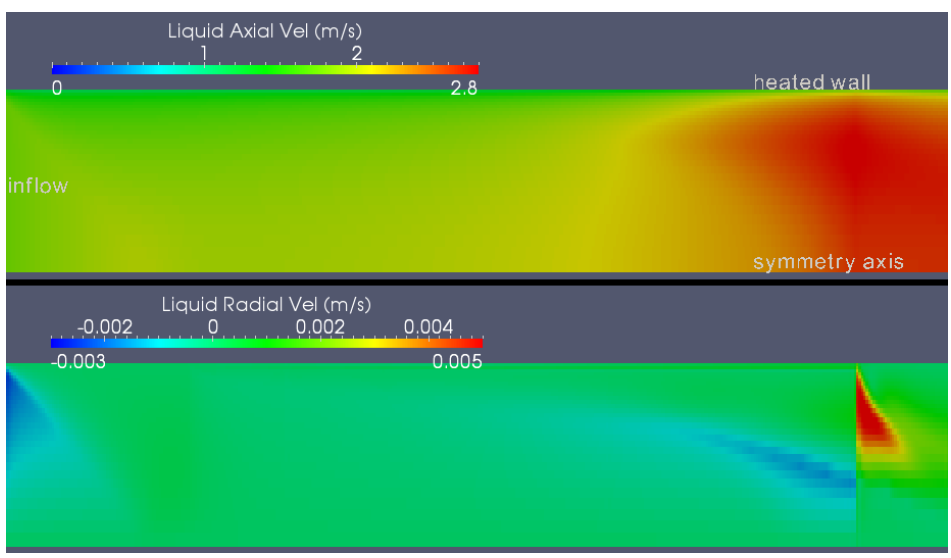

Figure 4: Nphase baseline solution for DEBORA problem. Top is axial velocity, bottom is radial velocity of the liquid phase.

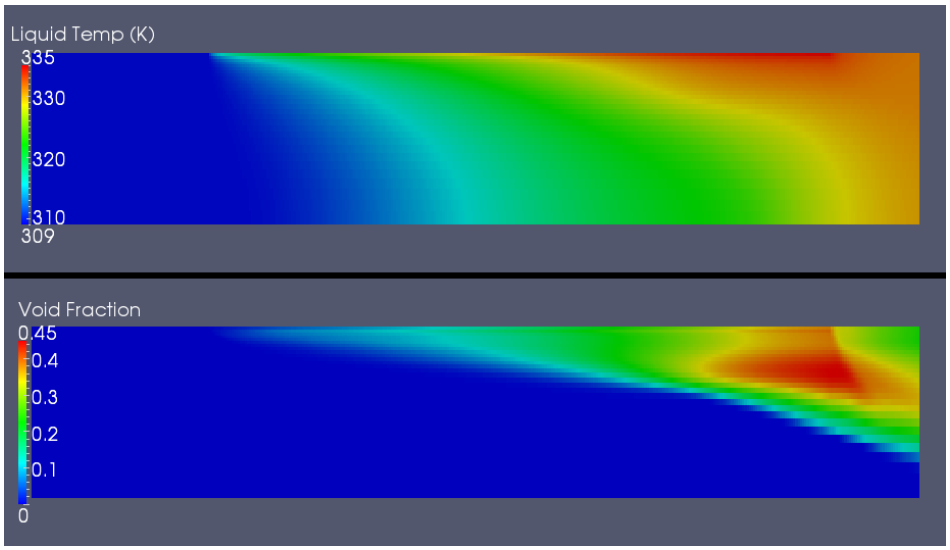

Figure 5: Nphase baseline solution for DEBORA problem. Top is temperature of the liquid, bottom is void fraction.

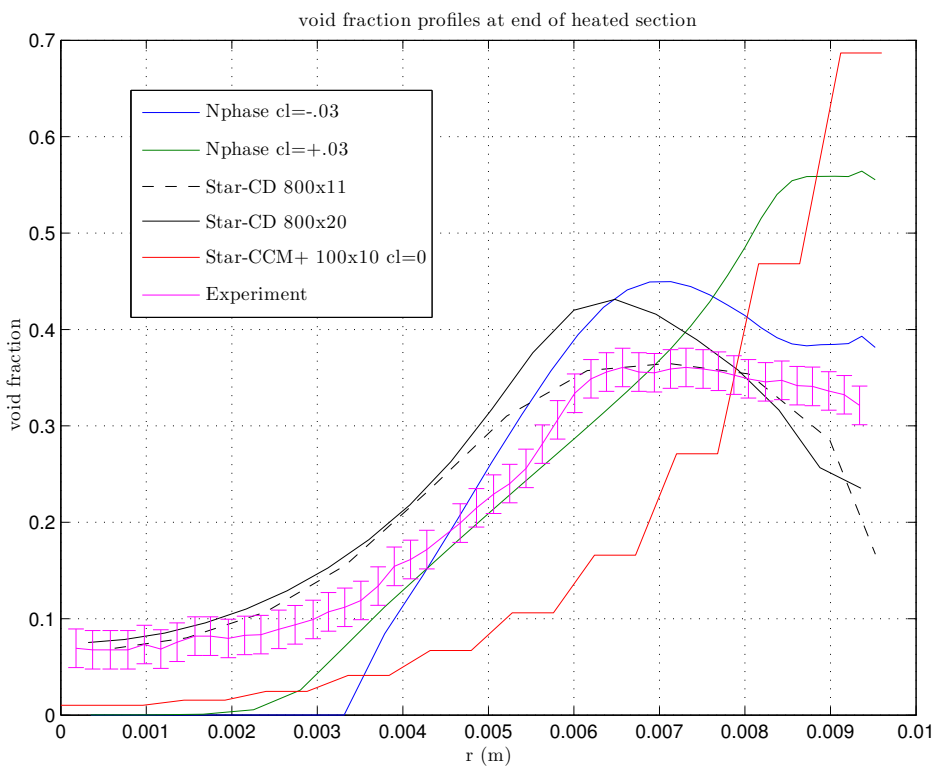

Figure 6: Comparison of void fraction profiles at the end of the heated section from various simulations and experimental data.

- Negligible effect of added momentum due to gas injection
- Successful alternate implementation of mass and energy transfer, similar to Star-CD implementation
- $C_L > 0$ hinders convergence, stabilized by setting $C_L(r > R - d_{\text{bubble}}) = 0$
- Radial velocity artifact at end of heated section is grid-independent and appears in Star-CD and Star-CCM+

4.2 Heat Partitioning Sensitivity Study

Since a sensitivity study was performed, it was necessary to see if parameter variations modify the wall heat partitioning profile that was taken from the Star-CD solution. Parameters with the strongest effect on outputs were C_L, d_{bubble}, and C_μ. A centered parameter study was performed to assess variability in the heat partitioning profile. Although the values of C_L in the Star-CD sensitivity study were conservative ($-0.03 \pm 30\%$), we now wish to explore a larger range of C_L. The literature survey suggests that $C_L \in [-0.3, 0.3]$, but Nphase does not converge well for $C_L \gtrsim -0.01$. Table 1 shows the parameters and ranges, and Figure 7 shows the resulting profiles. If we define q_l as the heat flux going into the liquid and q_g as the heat causing boiling, then the plot shows

$$\left(\frac{q_g}{q_l + q_g}\right) - \left(\frac{q_g}{q_l + q_g}\right)_{\text{baseline}} = \hat{q}_g - \hat{q}_{g,\text{baseline}}.$$

Thus, parameter variations cause at most a 3 percentage point change in the profile. This is the same order of magnitude as the interpolation error encountered in importing the profile into Nphase.

Table 1: parameters for sensitivity study of heat flux partitioning profile

Parameter	Range	Reasoning
C_L	$[-0.1, -0.01]$	required for convergence
d_{bubble}	$\pm 30\%$	used in Star-CD sensitivity study
C_μ	$\pm 30\%$	used in Star-CD sensitivity study

In order to see how much modified heat partitioning profiles affect the outputs of interest, Nphase was then run with the (four) heat partitioning profiles for the modified d_{bubble} and C_L. The parameters in Nphase remained at baseline, only the heat partitioning was changed. The resulting variation in the outputs is shown in Table 2. Previous work on the sensitivity of Star-CD showed that these variations in the outputs are small compared to variations in the outputs from directly altering parameters. Thus, it is sufficient to use the baseline heat partitioning profile for all Nphase runs, provided that output variations less than $\approx 2\%$ are deemed insignificant.

4.3 Preliminary Sensitivity Study

Using the baseline DEBORA solution as the initial condition, a preliminary sensitivity study was performed to verify that the relevant physics were being captured by Nphase. In addition, the study was done to test the link between Nphase and Dakota. Latin-Hypercube samples were generated for four simple parameters that would have strong and obvious effects on the solution.

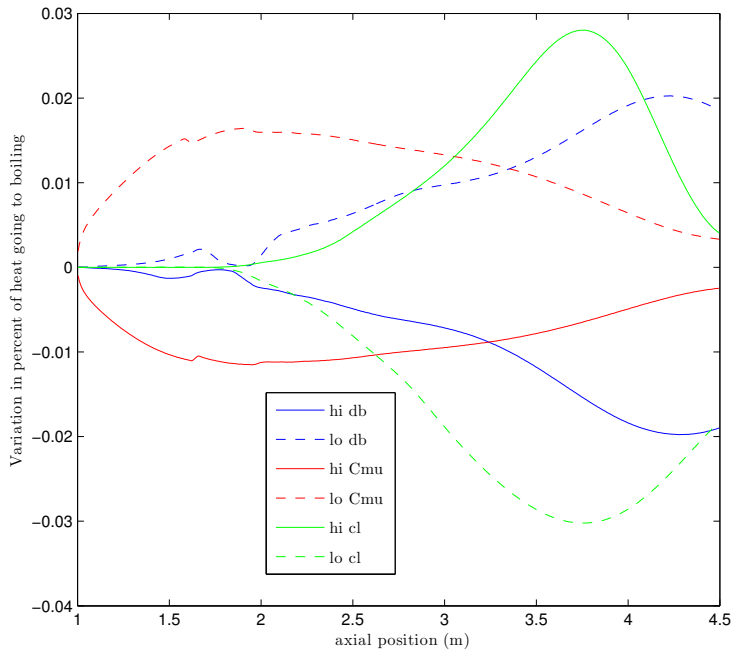

Figure 7: variation of heat partitioning profile from Star-CD DEBORA solution.

Table 2: variation in outputs for different heat partitioning profiles.

	Δp	$\overline{T}_{\text{wall}}$	$\overline{\alpha}$	$\overline{r}_\alpha$
C_L	0.03%	0.07%	2%	0.4%
d_{bubble}	0.005%	0.05%	0.4%	0.15%

The parameters were acceleration due to gravity, overall magnitude of heat flux, magnitude of mass flux, and inlet velocity. Each parameter was varied by ±30%. The correlation coefficients between the parameters and outputs are shown in Figure 8.

The sensitivity shows that Nphase correctly identifies gravity as having a strong effect on pressure drop and little effect on other parameters. The positive correlation of heat flux with wall temperature and void fraction shows that increasing heat flux will make the wall hotter and generate more gas, as expected. Also, it will move the centroid of the void fraction closer to the center of the pipe (where $r = 0$). The mass flux is shown to have a similar but weaker effect, and it does not affect the wall temperature. Finally, a large inlet velocity reduces wall temperature due to convective cooling, thereby also reducing void fraction. Large velocities also enhance the lift force, keeping the bubbles near the pipe wall.

The solution behaved as expected for all of the parameters. Also, the correlation coefficients give reasonable insight into how the parameters affect the outputs. The next step was to conduct a full sensitivity study on all of the parameters of interest.

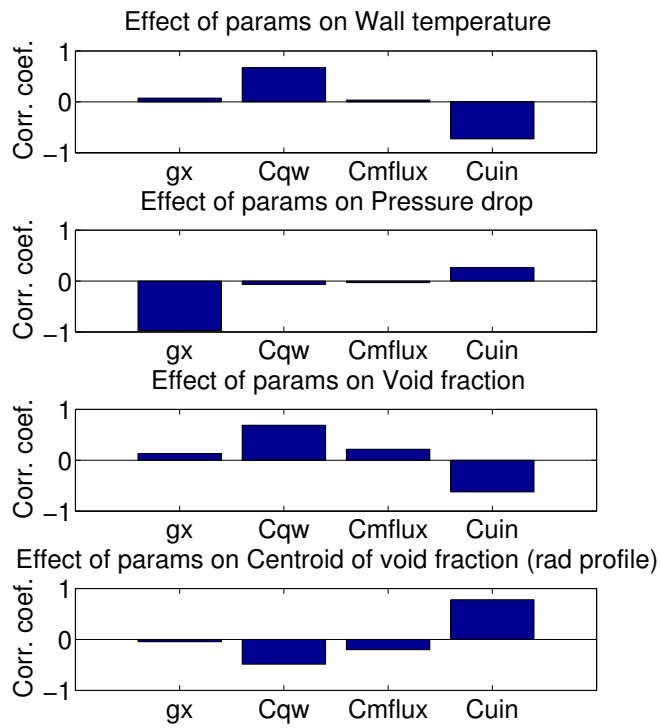

Figure 8: correlation coefficients between parameters and outputs for the preliminary sensitivity study.

5 Full Sensitivity Study

The full sensitivity study was performed using the same baseline solution as before. The heat partitioning profile was fixed to the baseline profile from Star-CD. After a literature survey, ten high-level parameters and appropriate ranges were chosen as shown in Table 3. The study had 1474 usable data points, which is more than the 1024 required for a full 2^k design. Each run in the study had 4000 iterations, and less than 8% of the runs diverged. The rest converged to the point where RMS(update)/RMS(state) $< 1\%$ for all states (except the radial velocity, for which we had looser requirements as explained earlier).

Figure 9 shows the correlation coefficients for the full sensitivity study. The plots clearly show that the bubble diameter and the turbulent dispersion coefficient have overwhelmingly large effects on the outputs, compared to the other parameters in the study. Interestingly, the bubble diameter has little effect on the average wall temperature. Both of these models have relatively little experimental evidence, yet have significant impact on the outputs.

By contrast, the lift, drag, and virtual mass forces, turbulence model, and wall heat partitioning model have little effect on the outputs, although many of these models are also lacking in experimental evidence. The heat partitioning model does indeed have a small effect (accounting for only 1.3% variation in the wall temperature), so we can be confident that it was reasonable to use a single heat partitioning profile for the entire study. The liquid Nusselt number seems to have a moderate effect on all of the outputs, but this model has enough evidence that time would be better spent improving other models.

Table 3: parameters and ranges for full sensitivity study.

Parameter	Symbol	Nominal	Range	Reasoning
lift coefficient	C_L	-0.03	$[-0.1, -0.01]$	required for Nphase convergence, [1]
drag coefficient	C_D	Wang fit	$\pm 30\%$	approximate experimental variation (no data for Wang fit itself) [2]
virtual mass coefficient	C_{VM}	1.0	$[0.5, 1.5]$	nominal values in Star-CD (see also [3]) and Nphase, and part of range from [4]
turbulent dispersion coefficient	C_{TD}	$2/3$	$[0.3, 1.5]$	encompasses much of range from [5] and calculated from Nphase solution using formula in [6].
bubble diameter	d	7×10^{-4}m	$[1.5, 20] \times 10^{-4}$m	range from Star-CD, Star-CCM+, Nphase, and [5].
lift force wall distance	$\hat{y}_{\text{wall}}$	1	$[1, 4]$	range for Star-CD, Nphase, and [1, 6, 7].
turbulent viscosity scaling	C_μ	0.09	$[0.07, 0.09]$	calculated for Nphase solution using formulas in [8–11].
liquid to interface Nusselt number	Nu_l	Modified Ranz-Marshall	$\pm 30\%$	approximate range for many experimental results [12–16].
gas to interface Nusselt number	Nu_g	analytic (see [17])	$[0, 50]$	encompasses much of analytic form in [17], data from [18], and Star-CD.
heat flux partitioning	$\hat{q}_g$	from Star-CD solution	$\pm 5\%$	heat partitioning sensitivity study (see above).

Figure 10 shows some scatter plots for the various outputs. Table 4 shows the ranges of the various outputs, which are probably too large for many engineering applications. The results from this study suggest that more sophisticated models for bubble diameter, such as single or multi-equation interfacial area transport models, are needed to accurately simulate two-phase flow. Also, more experimental work should be done to more carefully characterize the turbulent dispersion force.

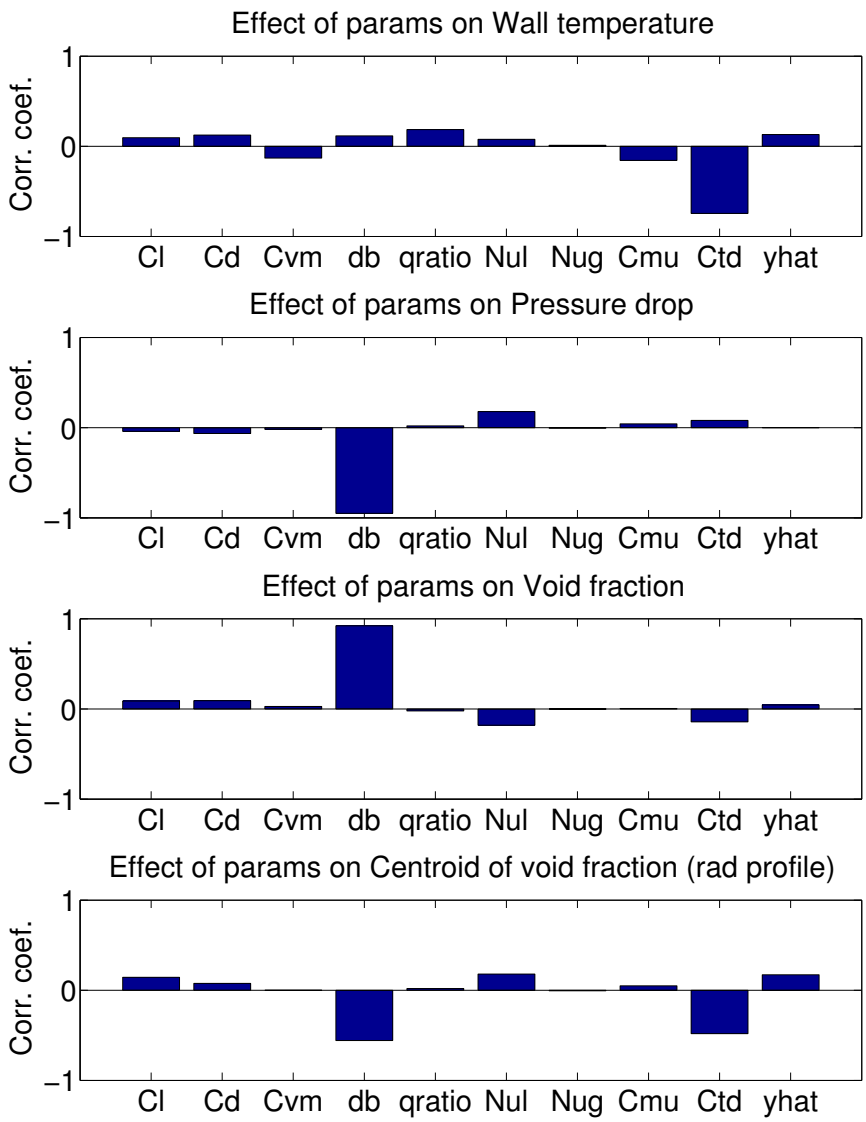

Figure 9: correlation coefficients between parameters and outputs for the full sensitivity study.

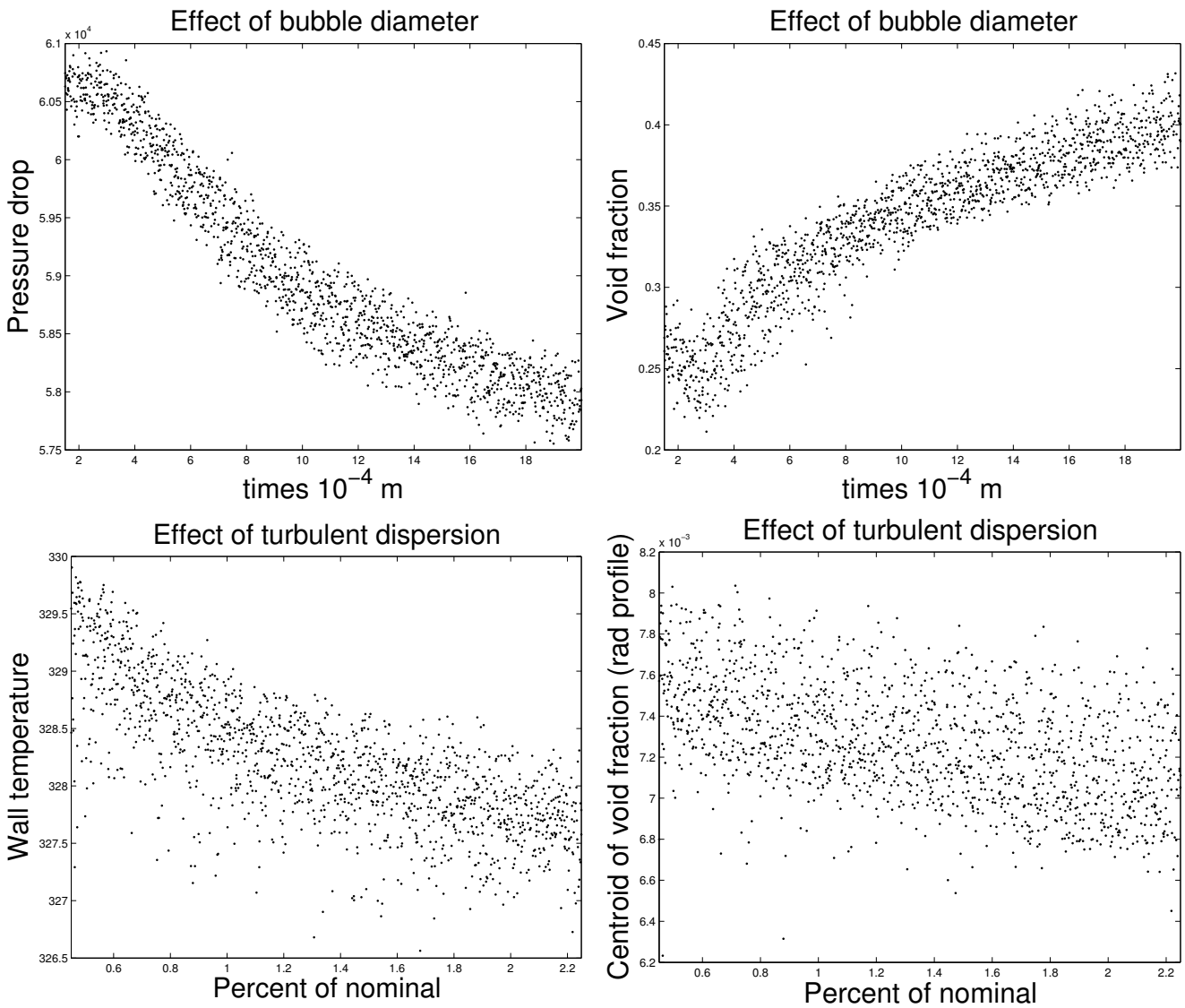

Figure 10: example scatter plots for the full sensitivity study.

Table 4: variation in outputs for full sensitivity study.

Δp	57.5-61 KPa
$\overline{T}_{\text{wall}}$	326.5-330 K
$\overline{\alpha}$	0.2-0.45
$\overline{r}_{\alpha}$	6.2-8.2 mm

6 References

[1] Akio Tomiyama, Hidesada Tamai, Iztok Zun, and Shigeo Hosokawa. Transverse migration of single bubbles in simple shear flows. *Chemical Engineering Science*, 57:1849–1858, 2002.

[2] D.G. Karamanev. Rise of gas bubbles in quiescent liquids. *AIChE journal*, 40(8):1418–1421, 1994.

[3] D. A. Drew and R. R. Lahey Jr. The virtual mass and lift force of a sphere in rotating and straining inviscid flow. *International Journal of Multiphase Flow*, 13(1):113–121, 1987.

[4] M. Lopez de Bertodano, RT Lahey, and OC Jones. Phase distribution in bubbly two-phase flow in vertical ducts. *International Journal of Multiphase Flow*, 20(5):805–818, 1994.

[5] W. Yao and C. Morel. Volumetric interfacial area prediction in upward bubbly two-phase flow. *International Journal of Heat and Mass Transfer*, 47(2):307–328, 2004.

[6] S. Hosokawa and A. Tomiyama. Multi-fluid simulation of turbulent bubbly pipe flows. *Chemical Engineering Science*, 64:5308–5318, 2009.

[7] SP Antal, RT Lahey Jr, and JE Flaherty. Analysis of phase distribution in fully developed laminar bubbly two-phase flow. *International Journal of Multiphase Flow*, 17(5):635–652, 1991.

[8] BE Launder and BI Sharma. Application of the energy-dissipation model of turbulence to the calculation of flow near a spinning disc. *Letters Heat Mass Transfer*, 1:131–137, 1974.

[9] BE Launder and DB Spalding. The numerical computation of turbulent flows. *Computer methods in applied mechanics and engineering*, 3(2):269–289, 1974.

[10] B. E. Launder, A. Morse, W. Rodi, and D. B. Spalding. Prediction of free shear flows – a comparison of the performance of six turbulence models. Technical report, NASA, 1973. Document ID: 19730019433.

[11] W. Rodi. *The prediction of free turbulent boundary layers by use of a two-equation model of turbulence*. PhD thesis, University of London, 1972.

[12] F. Mayinger and YM Chen. Heat transfer at the phase interface of condensing bubbles. In *Proc. of the 8th Int. Heat Transfer Conf*, volume 4, pages 1913–1918, 1986.

[13] YM Chen and F. Mayinger. Measurement of heat transfer at the phase interface of condensing bubbles. *International journal of multiphase flow*, 18(6):877–890, 1992.

[14] J. Isenberg and S. Sideman. Direct contact heat transfer with change of phase: bubble condensation in immiscible liquids. *International Journal of Heat and Mass Transfer*, 13(6):997–1011, 1970.

[15] O. Zeitoun, M. Shoukri, and V. Chatoorgoon. Interfacial heat transfer between steam bubbles and subcooled water in vertical upward flow. *Journal of heat transfer*, 117:402, 1995.

[16] G.R. Warrier, N. Basu, and V.K. Dhir. Interfacial heat transfer during subcooled flow boiling. *International journal of heat and mass transfer*, 45(19):3947–3959, 2002.

[17] D.R. Shaver, S.P. Antal, M.Z. Podowski, and D. Kim. Direct steam condensation modeling for a passive PWR safety system. In *OECD Nuc. Energy Agency and IAEA Workshop, Sept. 2010, Washington D.C.*, 2010.

[18] RI Nigmatulin, NS Khabeev, and FB Nagiev. Dynamics, heat and mass transfer of vapour-gas bubbles in a liquid. *International Journal of Heat and Mass Transfer*, 24(6):1033–1044, 1981.

Part 2

Validation of STAR-CD and STAR-CCM+ boiling models against PBST and DEBORA experimental data

by

Victor Petrov, Timothy P. Grunloh, Timothy J. Drzewiecki, Isaac M. Asher,
Annalisa Manera, Krzystof J. Fidkowski

1 Introduction

This second part of the report is focused on the validation of the boiling models currently implemented in the CD-ADAPCO codes STAR-CD and STAR-CCM+. Experimental data from the DEBORA campaign and the OECD/NEA PSBT international benchmark have been used for the validation.

2 STAR-CD and STAR-CCM+ boiling model

A detailed description of the base boiling model implemented in STAR-CD and STAR-CCM+ is reported in Ref. [1]. The base model employs the Kurul and Podowski [2] formulation for the estimation of the bubble size distribution. A more sophisticated model for the bubble size distribution, called S-gamma, is also available in the STAR-CD and STAR-CCM+ implementation. The S-gamma model, consisting of a one-group interfacial area density transport equation, is described in details in Ref. [3]. For all the simulations presented in this report, the lift force and the virtual mass force have not been taken into account.

3 OECD/PSBT Benchmark Description

The NUPEC test facility depicted in Figure 1 consists of a high pressure and high temperature recirculation loop, a cooling loop, and instrumentation and data recording systems. The recirculation loop consists of a test section, circulation pump, preheater, steam drum (acting as a pressurizer), and a water mixer. The design pressure is 19.2MPa and the design temperature is 362 °C. The operating conditions of the test facility are reported in Table 1. An accuracy of ± 4% in absolute void fraction is specified for the measured data. A complete list of the experimental tests boundary conditions is reported in Appendix A.

Table 1 - Range of NUPEC PWR Test Facility Operating Conditions [4]

Quantity	Range
Pressure	4.9-16.6MPa
Mass velocity	550-4150kg/m^{2}s
Inlet coolant temperature	140-345°C

The coolant flows in the pressure vessel horizontally through the coolant inlet nozzle located just below the heated section. Experiments were performed with different test sections, representing a central subchannel with thimble, a side subchannel, and a corner subchannel respectively. The effective heated length is 1555 mm, and the void measurements were carried out 1400 mm downstream of the bottom of the heated section [4].

A gamma-ray transmission method was used to measure the density of the flow, which was converted into a void fraction measurement of the two-phase flow mixture. The measurement accuracy of the subchannel cross-section averaged void fraction is 4% (absolute void). The

measurement of the void distribution were performed on four different test sections, each representing a typical fuel assembly subchannel. The cross-sectional view of the four subchannels is shown in Figure 2.

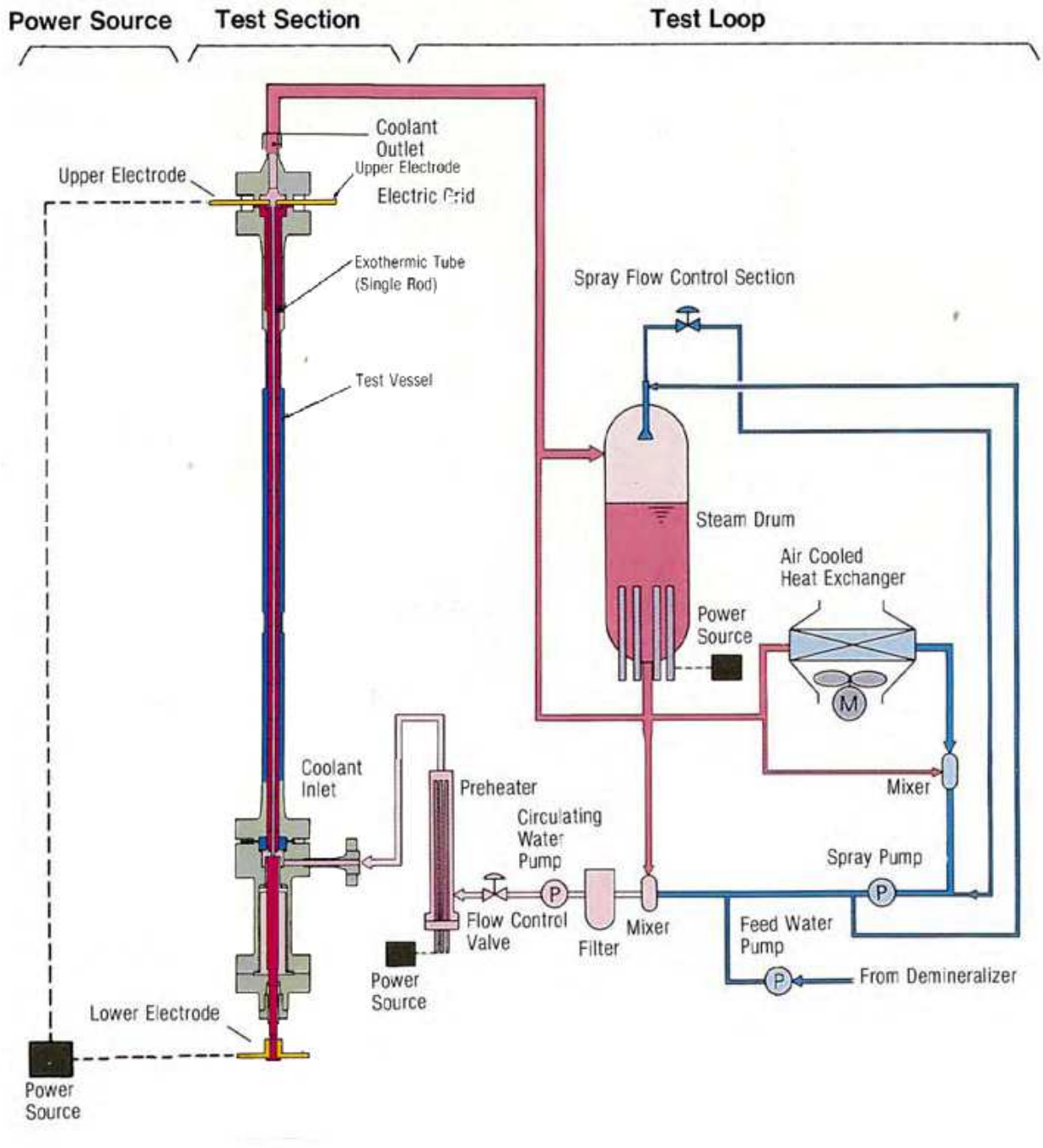

Figure 1 NUPEC test facility

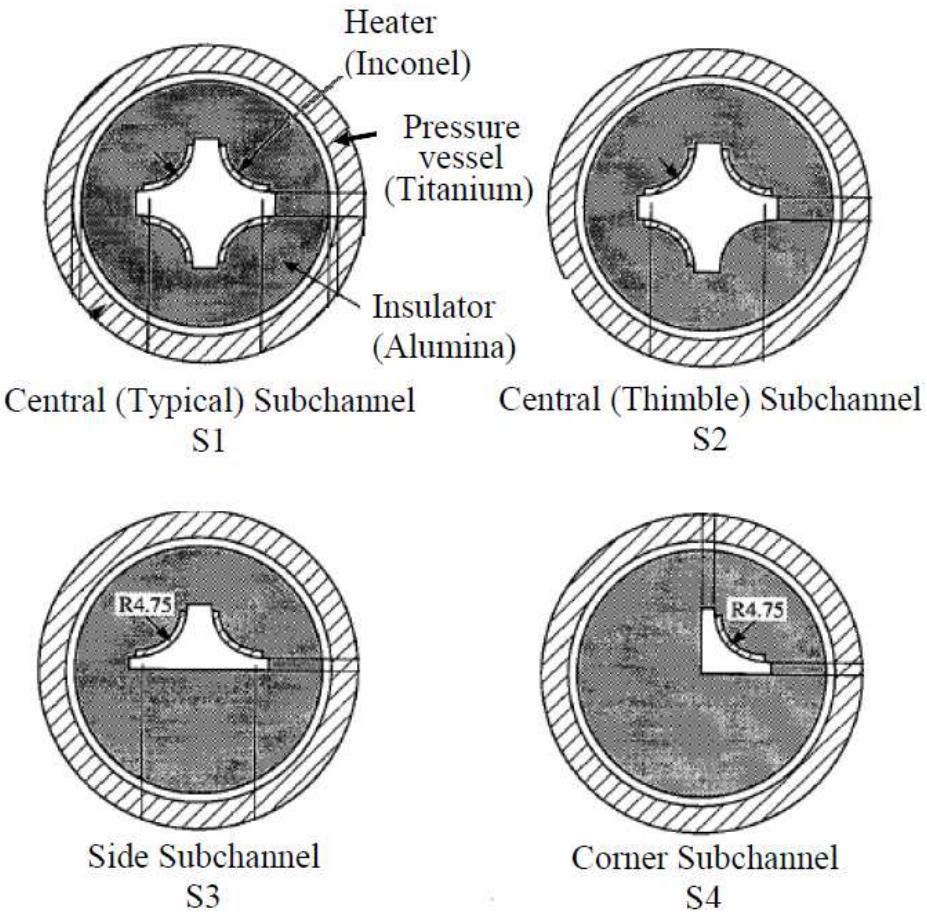

Figure 2 Cross Sectional View of Subchannel Test Assembly

4 CFD Model

The CAD model for the four PSBT subchannel sections is shown in Figure 3. The heated walls of the test section are indicated in red.

Because of the symmetry in the subchannels geometry, the flow domains could be modeled as 1/8 for S1, 1/2 for S2, 1/2 for S3 and 1/2 for S4 respectively (see Figure 4). Since the shape of the test section does not change in the axial (Z) direction, the CFD mesh can be built by extrusion of the 2D section mesh. Hexahedral 2D meshes were created utilizing the PROSTAR [5] internal scripting language. Polyhedral 2D meshes were created using the STAR-CCM+ mesher.

All meshes used in this study are illustrated in Figure 4. Each mesh contains 100 layers in the axial (Z) direction. A mesh sensitivity study was performed for the typical central subchannel geometry (S1) and has shown that the results were no longer affected when the amount of cells in the 1/8 S1 cross-section was increased beyond 250 cells. In order to achieve a smooth cells distribution to take into account for the fine cells close to the wall, the mesh selected for the S1

test case contains 536 cells per cross section. The results of the mesh convergence study were consistent with the findings of a mesh sensitivity study performed in a previous study [5].

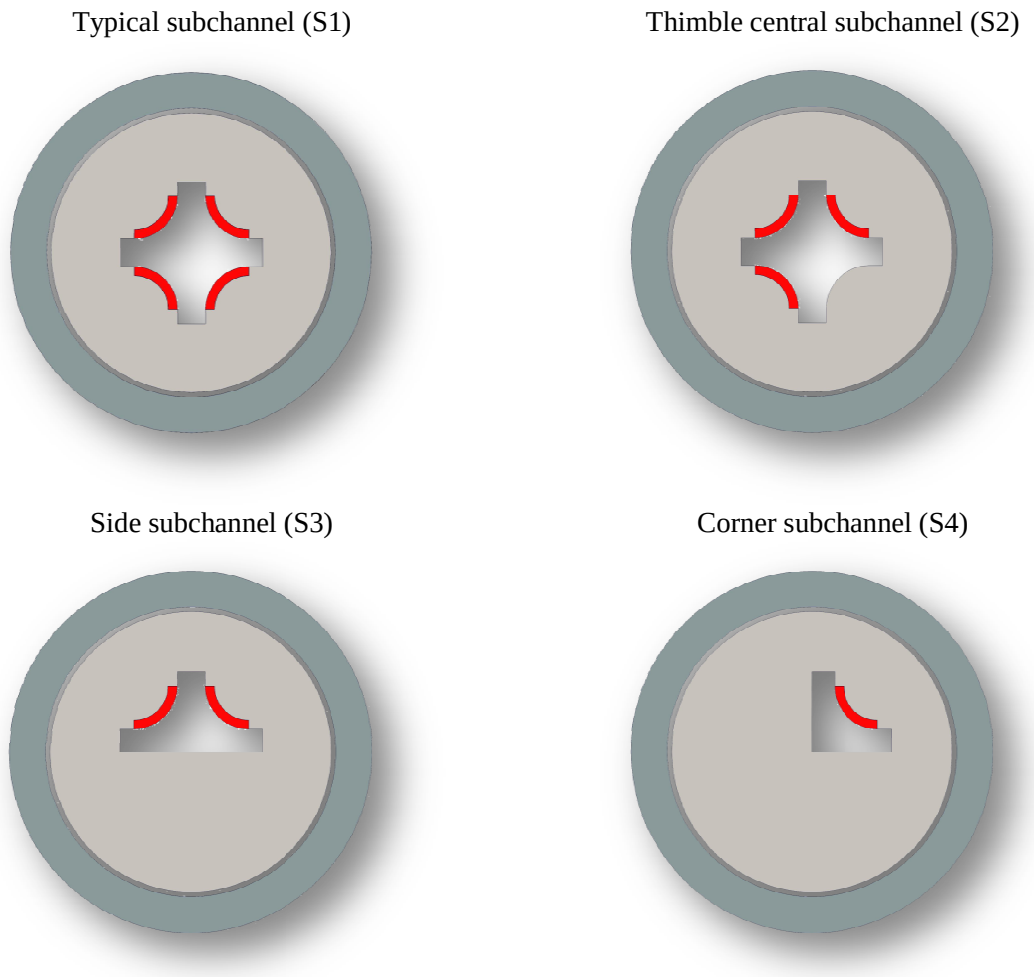

Figure 3 CAD models for the PSBT Subchannel test sections

The hexahedral CFD meshes consist of 53600 cells for the S1 test section type, 214400 cells for S2, 115800 cells for S3, and 62200 cells for S4 respectively. In addition, a polyhedral mesh of 79400 cells was built for the S1 test section type using cells base size close to hexahedral cells size for correspond subchannel geometry.

The boundary conditions employed for the CFD simulations is illustrated in Figure 5 (S1 subchannel case). These include imposed uniform fluid velocity profile and pressure for the inlet and outlet section respectively. Constant heat flux is imposed in correspondence of the heated walls. The unheated walls are modeled as adiabatic, and symmetry boundary conditions were applied were necessary. A flat inlet velocity profile was used, since no information about the inlet manifold geometry was supplied with the benchmark specifications.

Typical central subchannel S1 (1/8 symmetry)

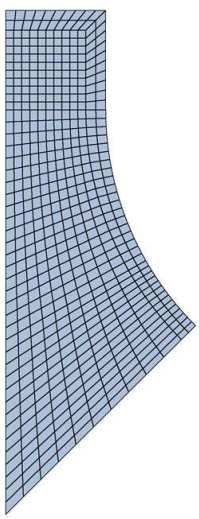

Hexa - 53600 Cells

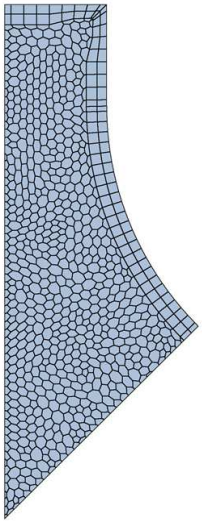

Polyhedral - 79400 Cells

Thimble central subchannel S2 (1/2 symmetry)

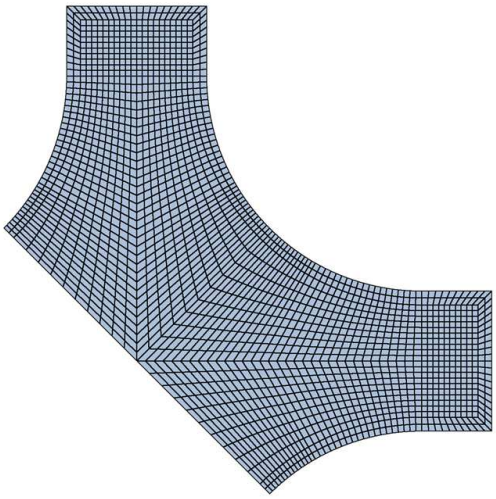

214400 Cells

Side subchannel S3 (1/2 symmetry)

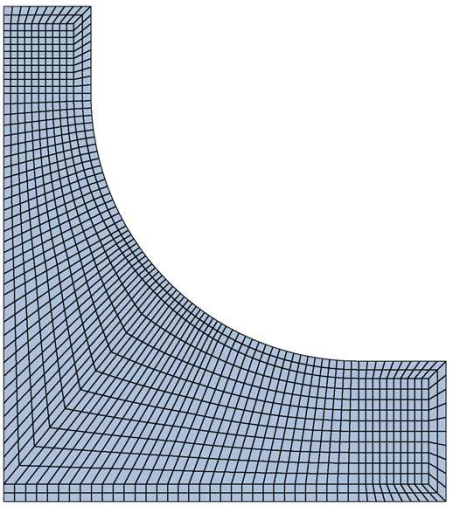

115800 Cells

Corner subchannel S4 (1/2 symmetry)

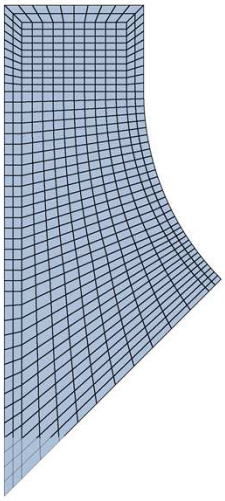

62200 Cells

Figure 4 Computational meshes

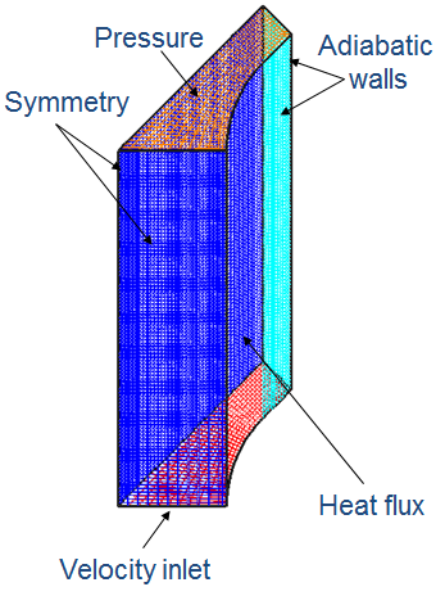

Figure 5 CFD Model Boundary Conditions (S1 Subchannel)

It is important to notice that the parameters of the numerical algorithm (i.e. relaxation factors, difference scheme, etc.) were not adjusted from run to run, and were kept the same for all geometries of the benchmark exercise. This is of relevance since the aim of the DOE/CASL project is to employ those models for more complex studies (fuel assemblies, full core, etc.), which involve multiple subchannels subjected to different boundary conditions. Therefore, the stability of the numerical scheme over a wide range of conditions and geometries is crucial.

5 Results of validation against PSBT experimental data

Base model

The entire set of NUPEC PWR experimental data made available within the OECD/NEA PSBT Benchmark were used in this study (see Appendix A for a complete list of the computed test cases). The results obtained by means of the STAR-CD and STAR-CCM+ base models (i.e. without S-gamma) using the hexahedral meshes reported in Figure 4 are presented in Figure 6 to Figure 9. Here the red lines represent the uncertainty bounds (± 4% absolute void fraction) for the measured cross-section averaged void fraction.

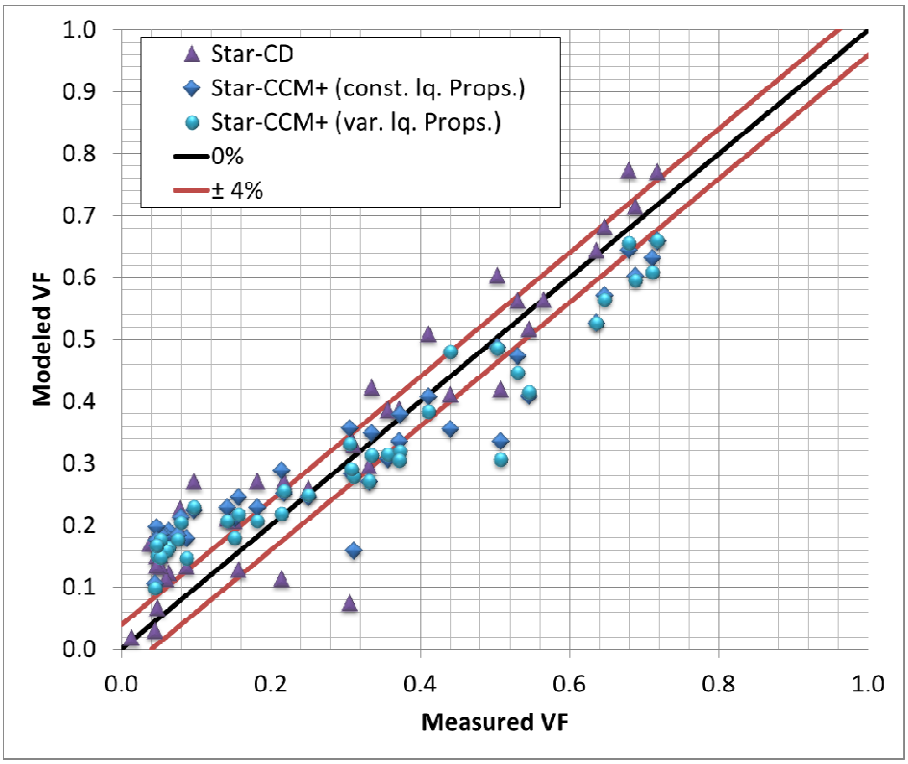

Figure 6 PSBT typical central subchannel S1

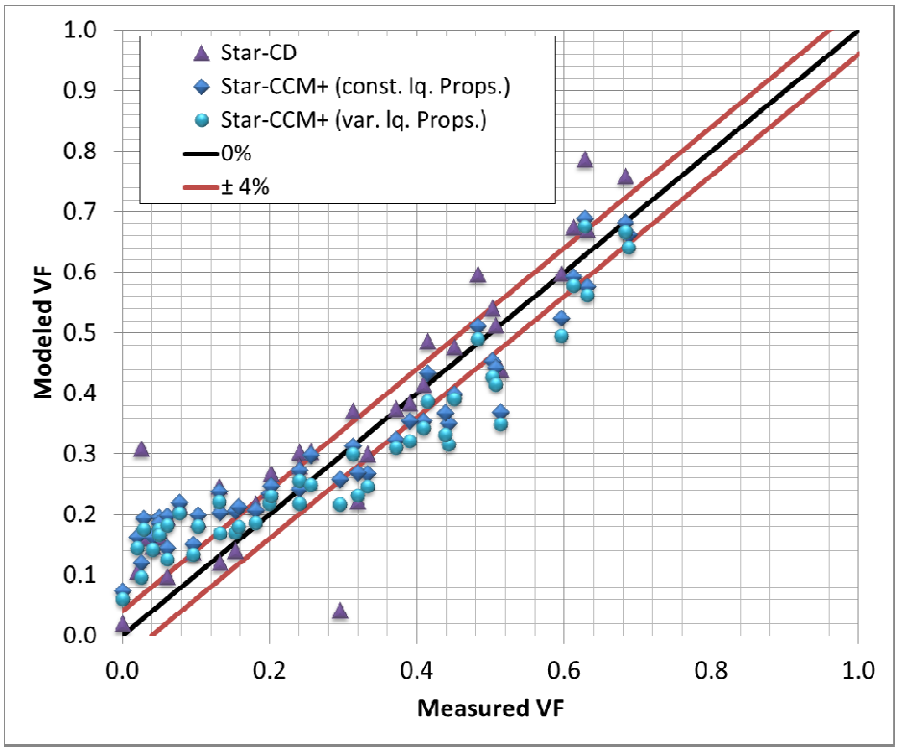

Figure 7 PSBT thimble central subchannel S2.

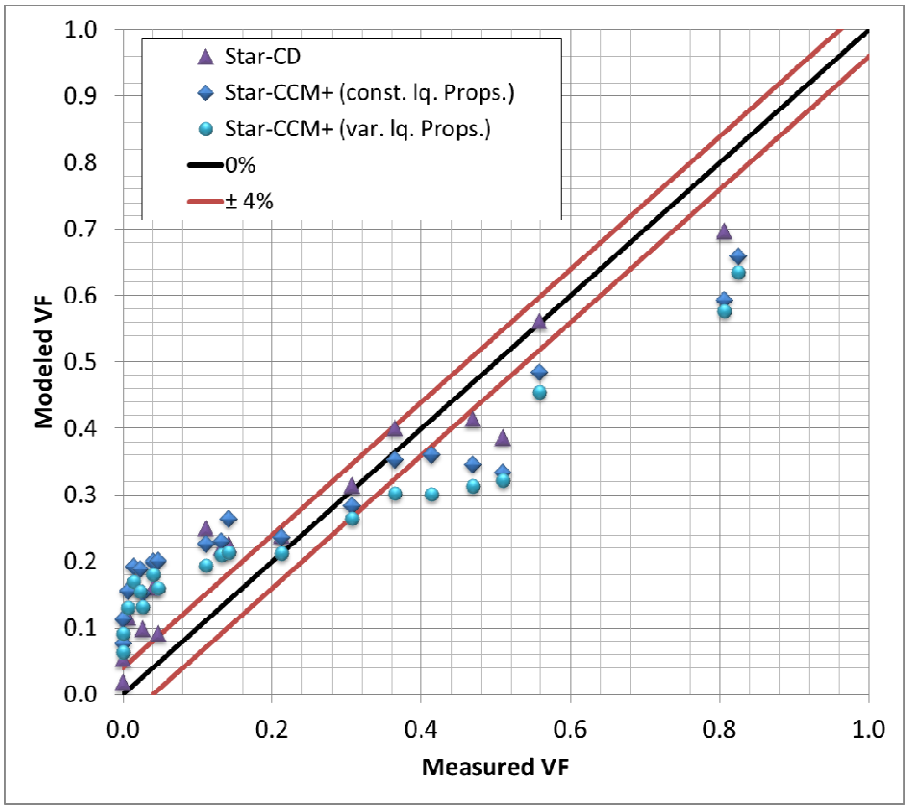

Figure 8 PSBT side subchannel S3

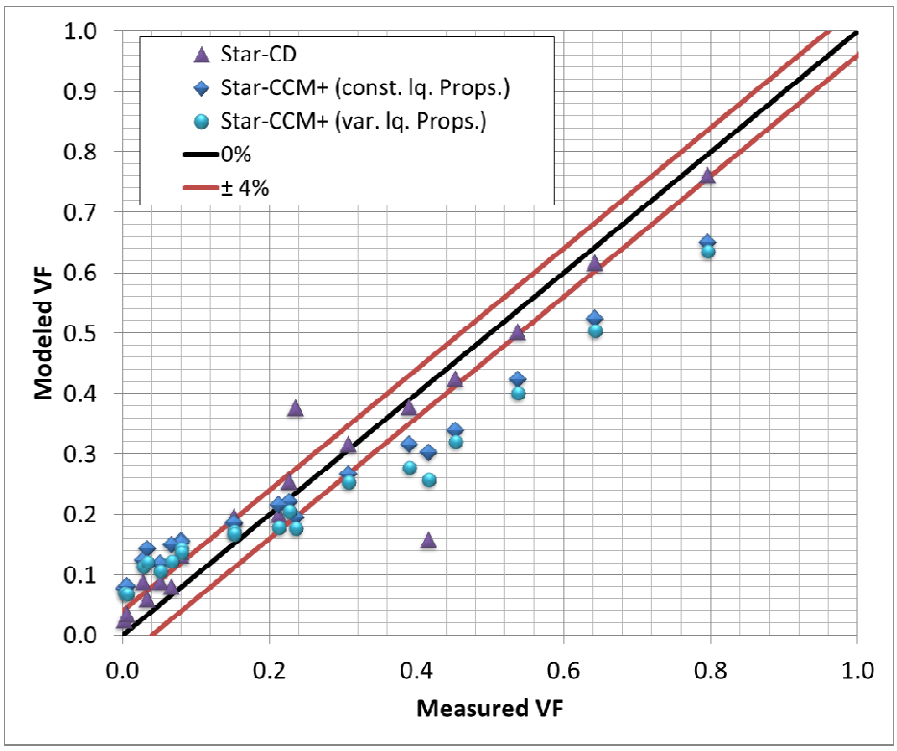

Figure 9 PSBT corner subchannel S4

All STAR-CD simulations were performed by employing variable liquid fluid properties. The effect of employing variable liquid thermodynamic properties (as function of local pressure and temperature) has been investigated by performing two sets of STAR-CCM+ simulations. At this aim, variable fluid properties based on the NIST steam/water tables have been implemented in STAR-CCM+ by means of use-defined internal tables.

In general it can be observed that a systematic overestimation of the void fraction is observed in the low void fraction range, while an underestimation of the void fraction is found in correspondence to the higher void fraction range. One of the main reasons for this discrepancy lies in the modeling of the bubble size, currently based on the Kurul and Podowski formulation [2]. A too large bubble size is predicted in the low void fraction range. This results in an underestimation of the condensation rate, which yield a too high void fraction. In the high void fraction range a too low bubble size is predicted instead. This leads to an overestimation of the condensation rate, with consequent underestimation of the overall cross-section averaged void fraction. Clearly, a more sophisticated model to take into account the evolution of the bubble size along the test section is needed.

It is also evident that the effect of the dependence of the liquid thermodynamic properties on the local temperature should not be neglected. Surprisingly, differences were observed between the STAR-CD and STAR-CCM+ simulations, despite the same models have been selected for the two codes. These results are currently being discussed with the main developer of the CD-ADAPCO two-phase flow models (Dr. Simon Lo).

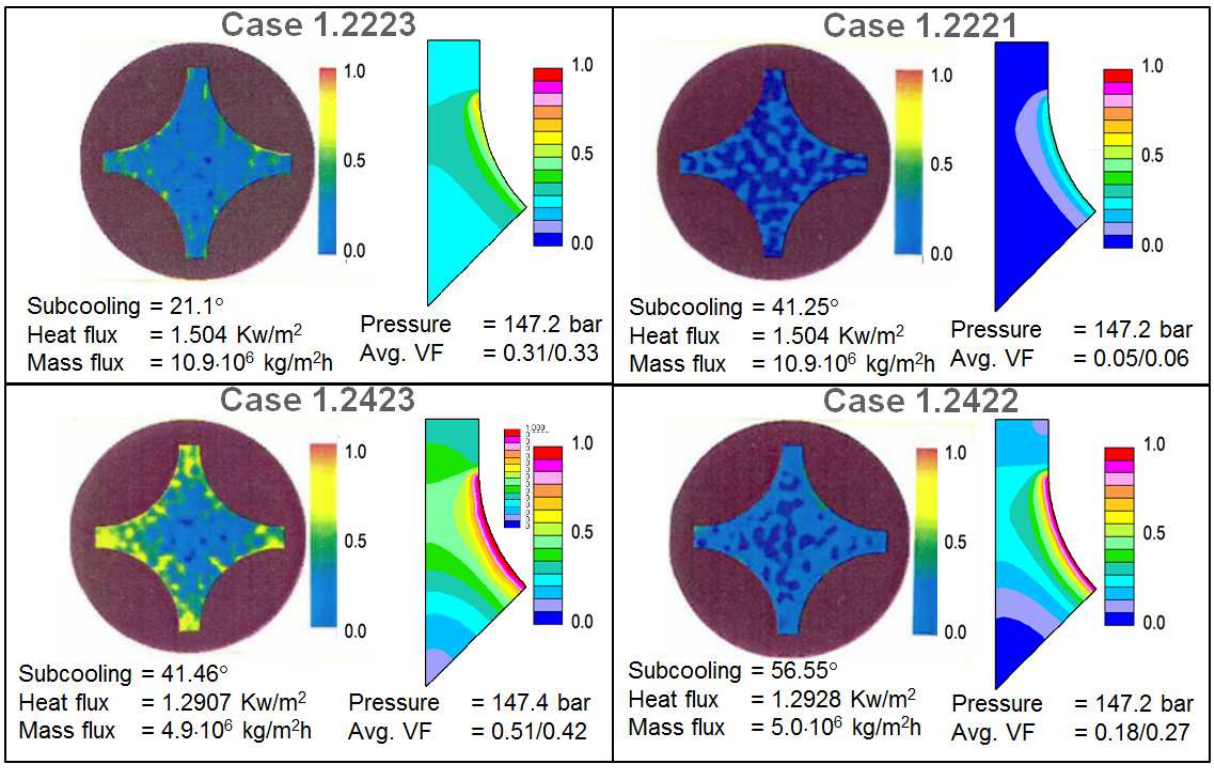

Figure 10 Radial void distribution for selected PSBT S1 test cases (central subchannel) obtained with STAR-CD (base model with variable liquid properties).

Figure 10

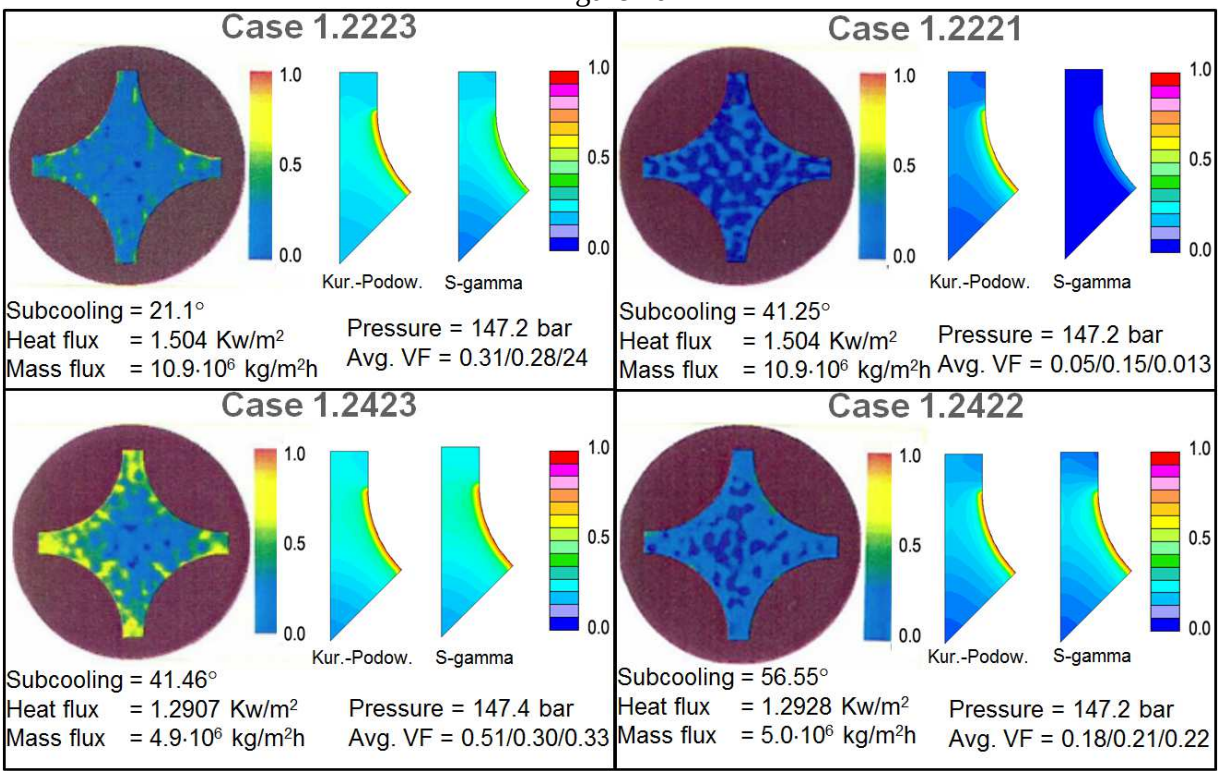

Figure 11 Radial void distribution for selected PSBT S1 test cases (central subchannel) obtained with STAR-CCM+ (variable liquid properties, with and without S-gamma).

In Figure 10 the radial void distribution in the measuring section is shown for selected PSBT S1 test cases. Here the experimental data (left figures) are reported together with the simulation results obtained with STAR-CD. Quantitative comparisons could not be performed, since only graphical data are available for the measured radial void distributions. In Figure 11 the same experimental cross-section void fraction distribution are compared with the results obtained with STAR-CCM+ using Kurul-Podowski and S-gamma respectively for the estimation of the bubbles size.

S-gamma

Recently, a mechanistic bubble size model (so-called S-gamma) for subcooled boiling flows has been proposed and implemented in STAR-CD and STAR-CCM+ [3]. This formulation is equivalent to the one-group interfacial transport area equation proposed by Prof. Ishii. The break-up and coalescence coefficients in the S-gamma transport equation have been adjusted on the basis of air-water experiments performed in Ishii's experimental laboratory [7] and DEBORA experimental data. The S-gamma model substitutes the simplified approach by Kurul and Podowski for the prediction of the bubble size distribution.

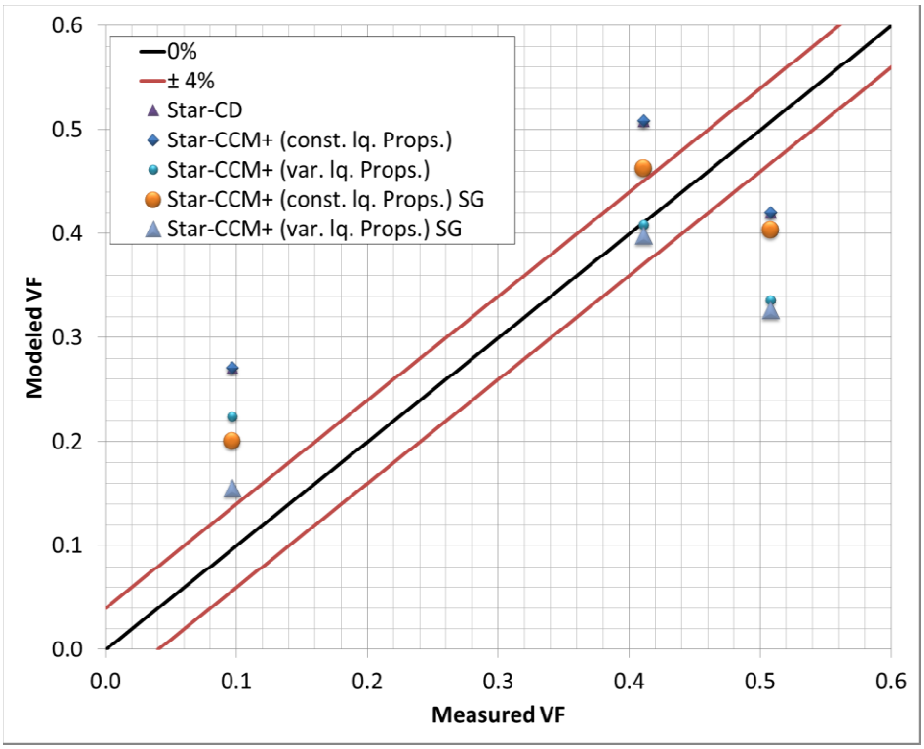

Figure 12 Effect of S-gamma modeling for selected S1 PSBT cases (1.2423; 1.4121; 1.522). Boundary conditions for the selected cases are reported in Appendix A.

The performance of the S-gamma model has been investigated against three selected PSBT test cases, 1.2423, 1.4121, and 1.522 of series S1 respectively (see Figure 12). The experimental test conditions for these cases are reported in Appendix A. The effect of variable liquid thermodynamic properties has been investigated in conjunction with the S-gamma model as well. Also in case of S-gamma formulation it is found that the dependence of the liquid thermodynamic properties with the local temperature cannot be neglected.

The results presented in Figure 11 clearly show that the employment of a more sophisticated model for the estimation of the bubble size distribution strongly contributes to the improvement of the prediction of the cross-section averaged void fraction in the low void fraction range. In the high void fraction range instead, the current S-gamma model has practically no effect (compare STAR-CCM+ results with variable liquid properties, with (purple triangle) and without (blue circles) S-gamma). Further improvements of the bubble coalescence and break-up terms are needed at high void fractions.

The effect of modeling the bubble size distribution using Kurul-Podowski and S-gamma formulations is presented in Figure 13 (with constant liquid properties) and Figure 14 (with variable liquid properties), where contour plots of the void fraction distributions in the simulated fluid domain are shown. The difference in void distribution is an indication of the higher condensation rate computed when the S-gamma model is activated. This is a direct consequence of the fact that S-gamma predicts smaller bubble sizes with respect to Kurul-Podowski's formulation.

PSBT 1.2423	
Kurul-Podowski 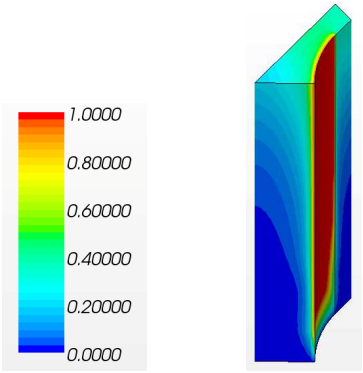 Avg. VF=0.33	S-gamma 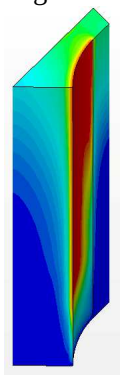 Avg. VF=0.40
PSBT 1.4121	
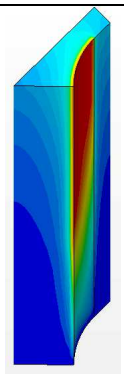 Avg. VF=0.22	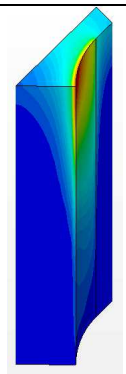 Avg. VF=0.20
PSBT 1.5222	
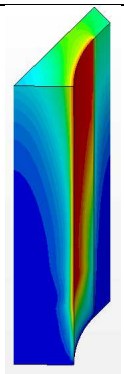 Avg. VF=0.40	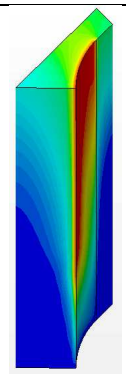 Avg. VF=0.46

Figure 13 Comparison of Star-ccm+ results obtained with Kurul-Podowski vs S-gamma (constant liquid thermodynamic properties).

PSBT 1.2423	
Kurul-Podowski 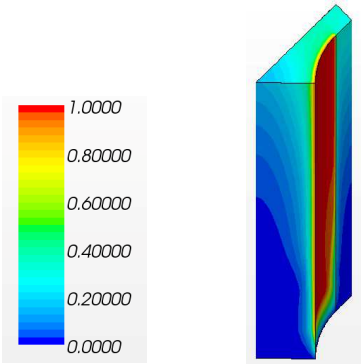 Avg. VF=0.30	S-gamma 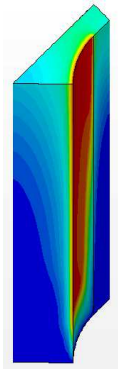 Avg. VF=0.32
PSBT 1.4121	
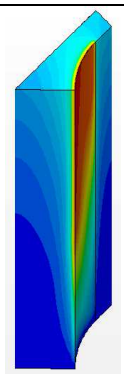 Avg. VF=0.22	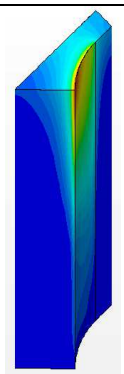 Avg. VF=0.15
PSBT 1.5222	
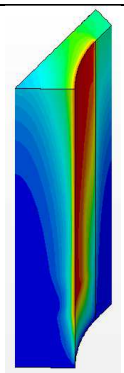 Avg. VF=0.38	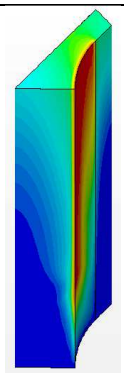 Avg. VF=0.39

Figure 14 Comparison of Star-ccm+ results obtained with Kurul-Podowski vs S-gamma (variable liquid thermodynamic properties - NIST water/steam tables).

Influence of the mesh type (hexahedral vs polyhedral cells)

Dependence of the void-fraction predictions on the type of CFD mesh was investigated as well. At this aim, a polyhedral mesh for the S1 type cross section was built, employing a similar cells size as used in the hexahedral mesh (detailed on the polyhedral mesh are given in chapter 4). The results obtained with the polyhedral mesh are reported in Figure 15. The cross-section averaged void fraction obtained with the polyhedral cells is about 1% (absolute void fraction) lower than the values calculated with the hexahedral cells. However, the numerical stability has notably deteriorated, as 41% of the analyzed cases did not converged, against a 10% of poorly converged cases resulting from the use of the hexahedral mesh. A relationship between numerical stability and void fraction values was not observed.

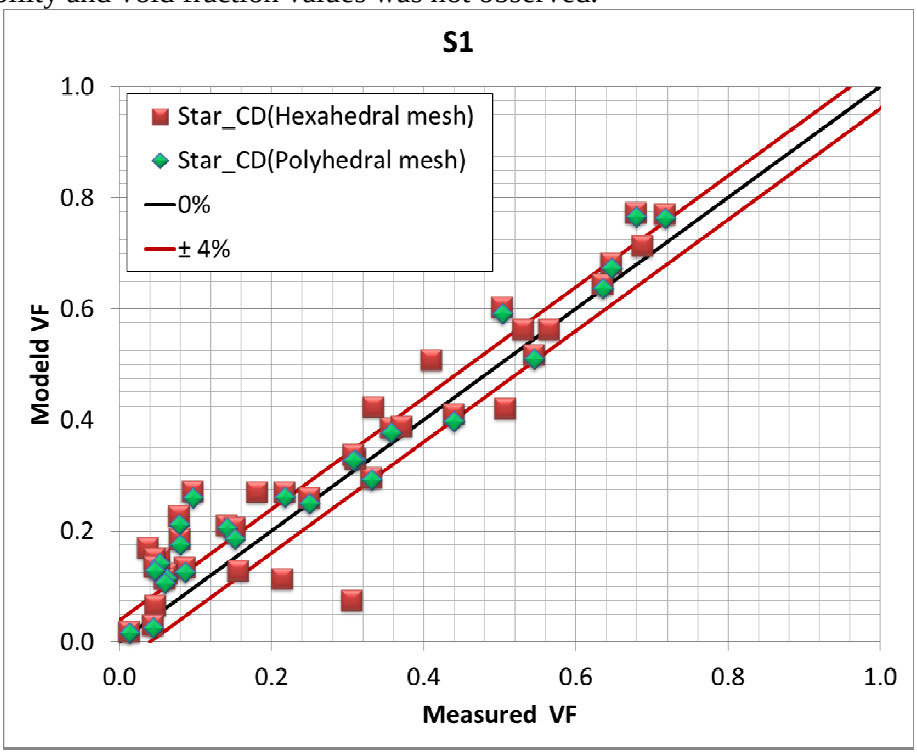

Figure 15 PSBT S1 test cases: STAR-CD base model predictions using a polyhedral and an hexahedral mesh respectively.

6 Description of the DEBORA experimental setup

In the DEBORA experimental campaign [8] Dichlorodifluoromethane (R12) was used as the working medium. The test section consists of a heated circular pipe having a inner diameter of 19 mm, and a heated length of 3.5 m followed by a 0.5 m adiabatic section. A scheme of the experimental set-up is shown in Figure 16. The operational conditions of the DEBORA test cases used in the present report for the validation of STAR-CCM+ and STAR-CD are listed in Table 2.

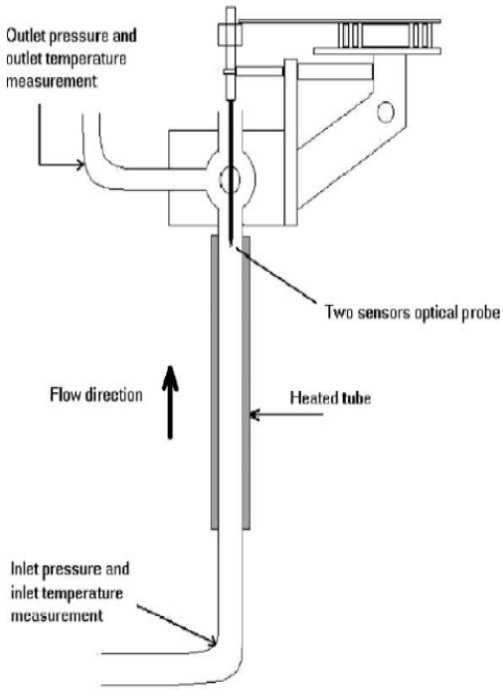

Figure 16 Scheme of the DEBORA experimental set-up

Table 2 - Selected test cases of the DEBORA experimental campaign

Case	Pressure, (bar)	Heat flux, (m/s)	V(inlet), (m/s)	T(inlet), (K)	Tsat, (K)
DEB5	26.15	73890	1.74	341.67	359.881
DEB6	26.15	73890	1.76	343.68	359.881
DEB10	14.59	76.24	1.59	308.06	331.218
DEB13	26.17	109420	2.63	342.35	359.921
S1	14.59	73161	1.56	301.67	331.218
S2	14.59	72054	1.57	304.3	331.218
S3	26.15	73151	1.71	335.88	359.881
S4	26.15	72722	1.76	343.68	359.881
DEB_C1	30.06	58260	0.83	326.12	367.356
DEB_C2	30.06	58260	0.84	331.54	367.356
DEB_C 3	30.06	58260	0.85	336.58	367.356
DEB_C 4	30.08	58260	0.88	341.04	367.392
DEB_C 5	30.07	58260	0.88	343.29	367.374
DEB_C 6	30.07	58260	0.90	345.8	367.374
DEB_C 7	30.06	58260	0.89	346.85	367.356

7 CFD model and mesh sensitivity

A 3D model based on quarter symmetry was developed for the simulation of the DEBORA experiments. A sketch of the model is illustrated in Figure 17 together with a representation of the imposed boundary conditions. A constant heat flux was applied to the heated wall. The

unheated wall section was modeled as adiabatic wall. A uniform velocity profile was imposed at the inlet of the test section, while a pressure boundary condition was imposed at the outlet section. Symmetry boundary conditions were applied on the remaining surfaces, as shown in Figure 17. The thermodynamic fluid properties have been evaluated on the basis of the NIST tables for R12.

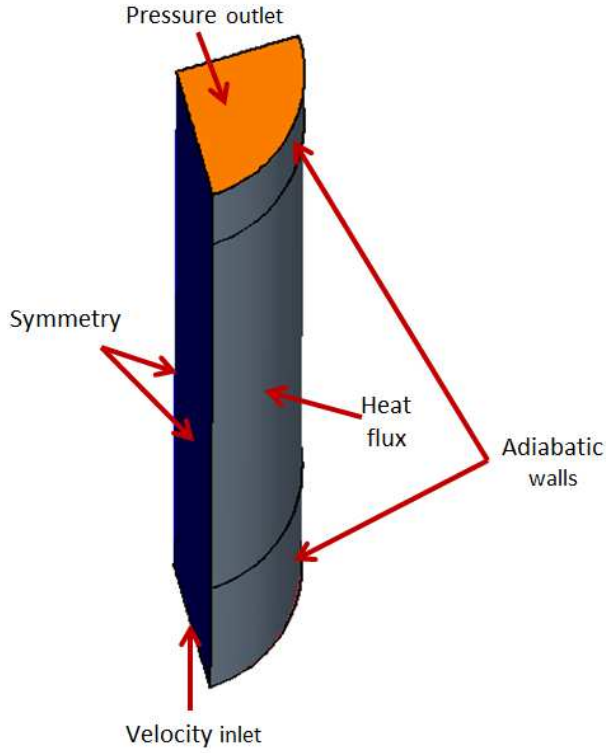

Figure 17 CFD model boundary conditions for DEBORA simulations

The CFD domain was meshed with hexahedral cells. A mesh convergence study was carried out on the basis of test case DEB5 reported in Table 2. The block structure of the mesh is shown in Figure 18. For the convergence study the number of cells in the central region (X1), in the periphery (X2) and in the boundary layer (X3) was varied, together with the number of axial cells. The results of the convergence study are presented in Table 3 for eleven different meshes. For each mesh the cross-section averaged void fraction corresponding to the measurements cross section is reported.

There is a large variation in inlet velocity (from about 0.82 m/s to about 2.6 ms) among the DEBORA cases considered in the present validation study. In view of this, it is not possible to fulfill the requirements on y+ for all DEBORA test cases with a single mesh. Therefore, two separate meshes were selected (V2 and V7 in Table 3), which results in y+ values close to 30 for both liquid and vapor phases for all DEBORA test cases analyzed in the present report. In particular, mesh V2 was used for DEB_C1 to DEB_C7 tests (for those cases V7 was yielding a y+ of about 25), while mesh V7 was employed for cases DEB5, DEB6, DEB10, DEB13, and DEB_S1 to DEB_S4.

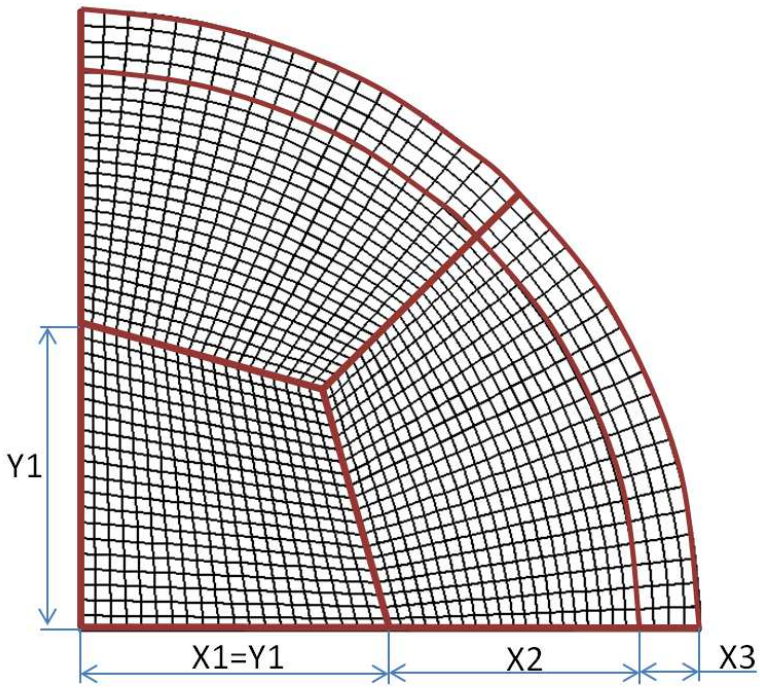

Figure 18 Block structured mesh (cells distribution) for DEBORA simulations

Table 3 - Mesh sensitivity study for DEBORA simulations

№	Axial	X1	X2	X3	Avg. VF
V1	200	10	10	2	0.3441
V2	200	20	20	4	0.3404
V3	200	40	40	8	0.2946
V4	400	20	20	4	0.3401
V5	200	40	40	4	0.3364
V6	800	20	20	4	0.3383
V7	200	20	20	8	0.2952
V8	1600	20	20	4	0.3364
V9	200	20	20	10	0.2907
V10	200	20	20	12	0.2865
V11	200	40	40	8	

The void fraction distributed computed for the DEB5 test case using different meshes is shown in Figure 19. The meshes V2 and V5 are characterized by the same number of cells in the boundary layer X3 (4 cells) and a different number of cells in the bulk region X1 (20 and 40 cells respectively). The meshes V3 and V7 are also characterized by the same number of cells in the boundary layer X3 (8 cells) and a different number of cells in the bulk region X1 (40 and 20 respectively). By comparing the results obtained for these four meshes (see Figure 19), it can be concluded that the results are rather insensitive to the mesh refinement in the bulk region of the flow, while the mesh refinement in the boundary layer plays a significant role.

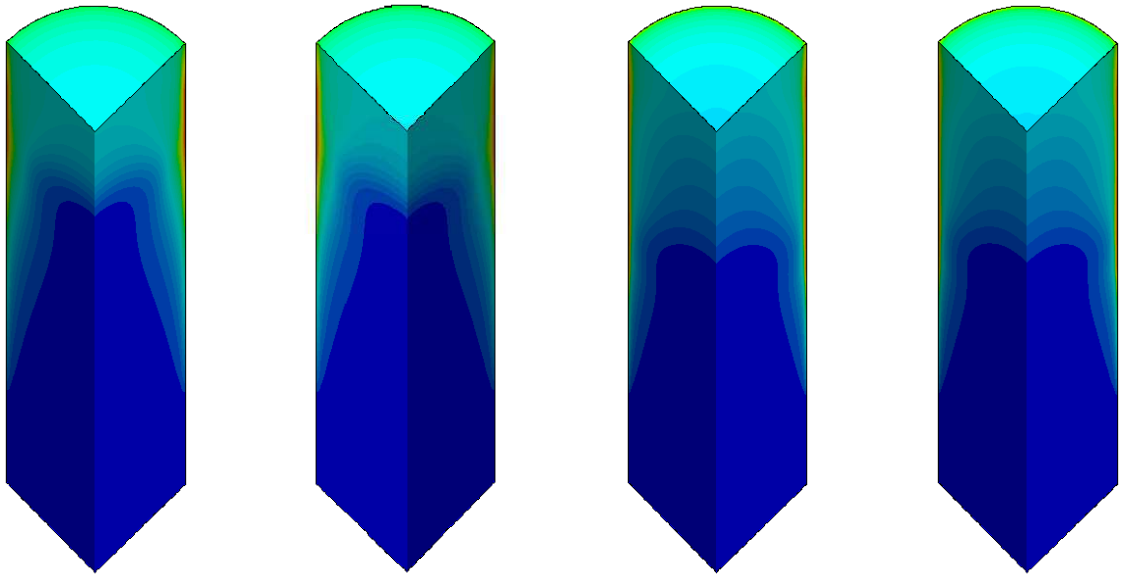

V2
272'000 Cells

V5
1'024'000 cells

V3
1'088'000 Cells

V7
304'000 Cells

Figure 19 Void fraction distribution for DEB5 test case obtained with different meshes

8 Validation results against DEBORA experimental data

The comparison between experimental and computed cross-section averaged void fraction for the DEBORA tests is reported in Figure 20. All results presented in this chapter have been obtained with STAR-CCM+. As for the PSBT benchmark, both base model (Kurul-Podowski) and S-gamma formulations have been analyzed. Mesh V2 or V7 (see table Table 3) has been employed in order to fulfill the y+ requirements of the specific test case. The results are consistent with the ones obtained for PSBT and discussed in chapter 5.

In Figure 21 to Figure 23 the void fraction profile is presented for three DEBORA cases (DEB10, DEB_C1 and DEB_c2 respectively) and the influence of employing constant vs variable liquid properties, or Kurul-Podoswki vs S-gamma formulation for the bubble size is illustrated. From Figure 21 it is evident that the S-gamma model has a considerable effect on the axial void fraction distribution. Smaller bubble size are generated when using S-gamma instead of Kurul-Podoswki, leading to a larger condensation rate in the lower part of the test section. This explains why with Kurul-Podowski a higher void fraction is calculated at low axial elevations. This effect is not observed in the upper part of the test section, where the void fraction measurements are performed. The effect of variable fluid properties is shown in Figure 22 and Figure 23.

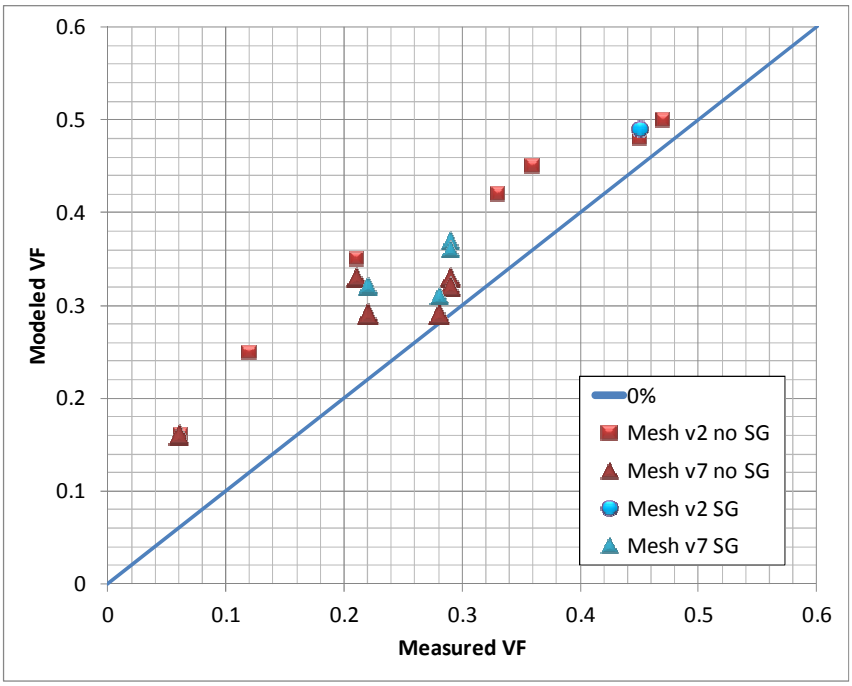

Figure 20 Comparison between measured and computed (STAR-CCM+) cross-section averaged void fraction for the DEBORA test cases listed in Table 2. Mesh V2 or V7 was used in order to fulfill the y+ requirements of the specific test case.

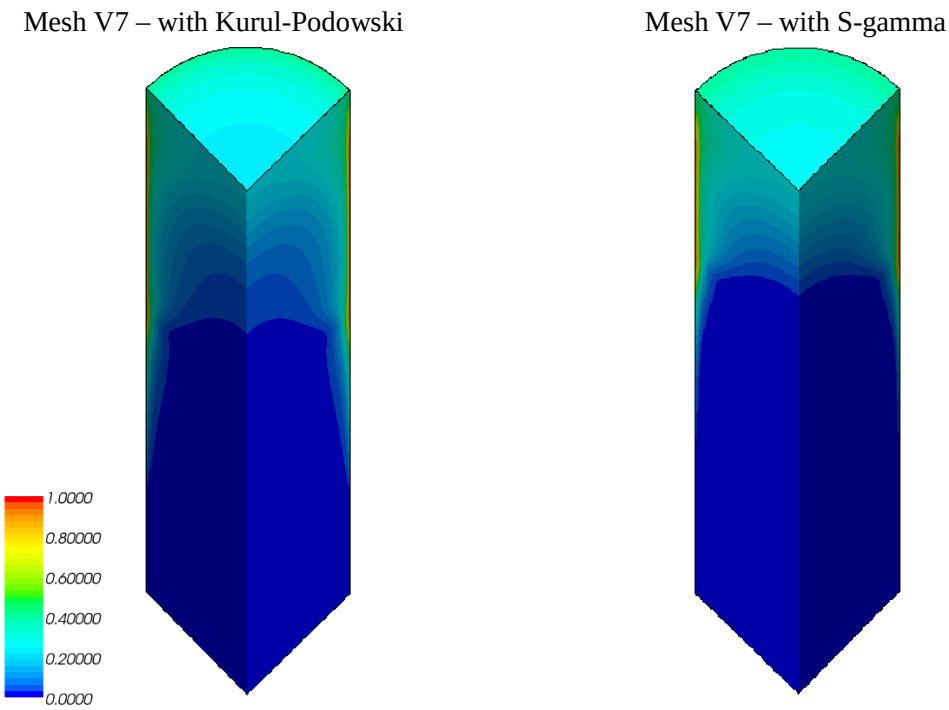

Figure 21 Void fraction distribution for DEB10 test case with Kurul-Podowski (left) and S-gamma (right) formulation for bubble size distribution (STAR-CCM+).

Mesh V2 – base model with constant lq. Properties Mesh V2 – base model with variable lq. Properties

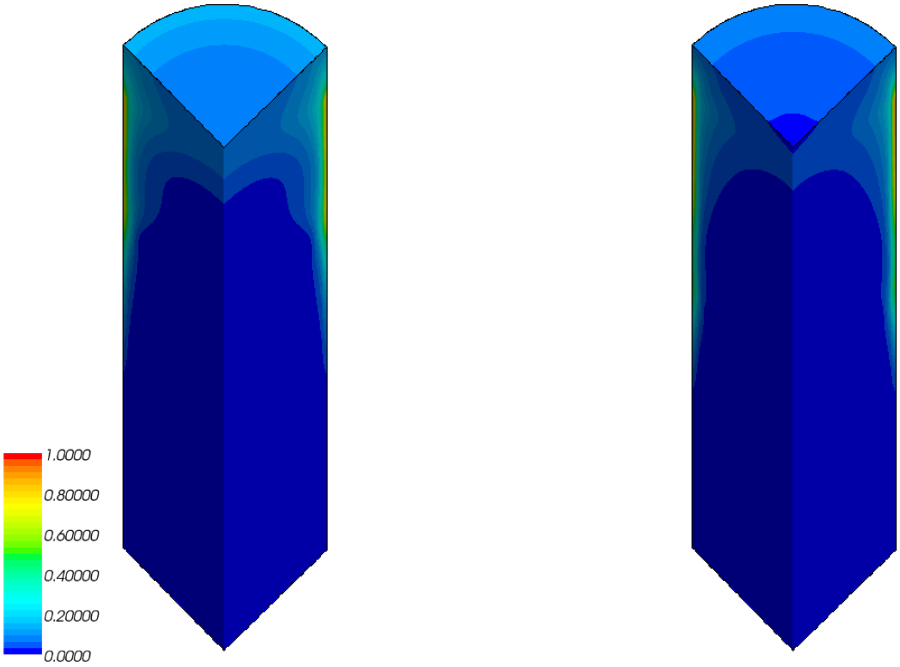

Figure 22 Void fraction distribution for DEB_C1 test case using STAR-CCM+ base model with constant (left) and variable (right) liquid thermodynamics properties.

Mesh V2 – base model with constant lq. Properties Mesh V2 – base model with variable lq. Properties

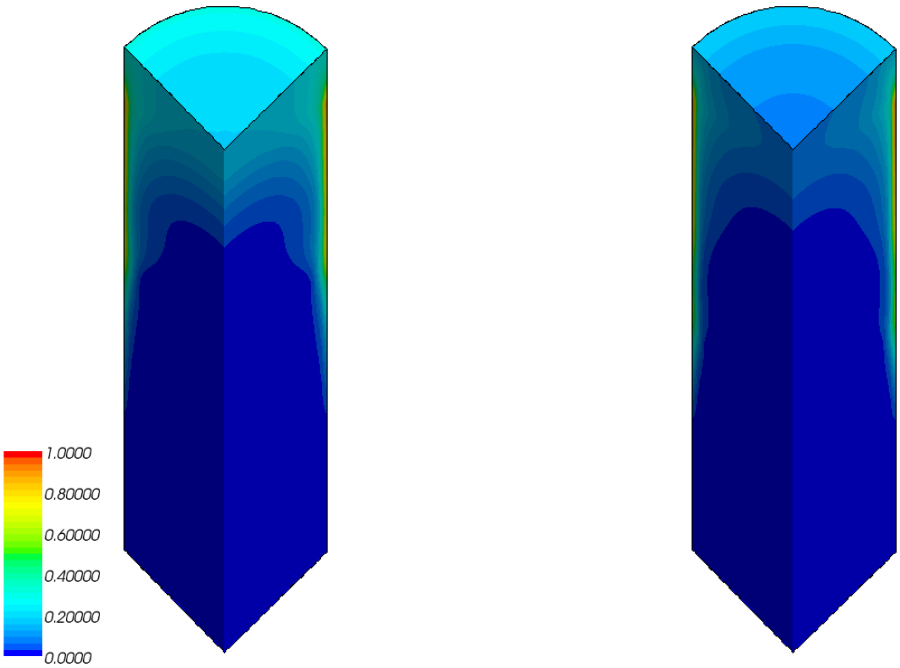

Figure 23 Void fraction distribution for DEB_C2 test case using STAR-CCM+ base model with constant (left) and variable (right) liquid thermodynamics properties.

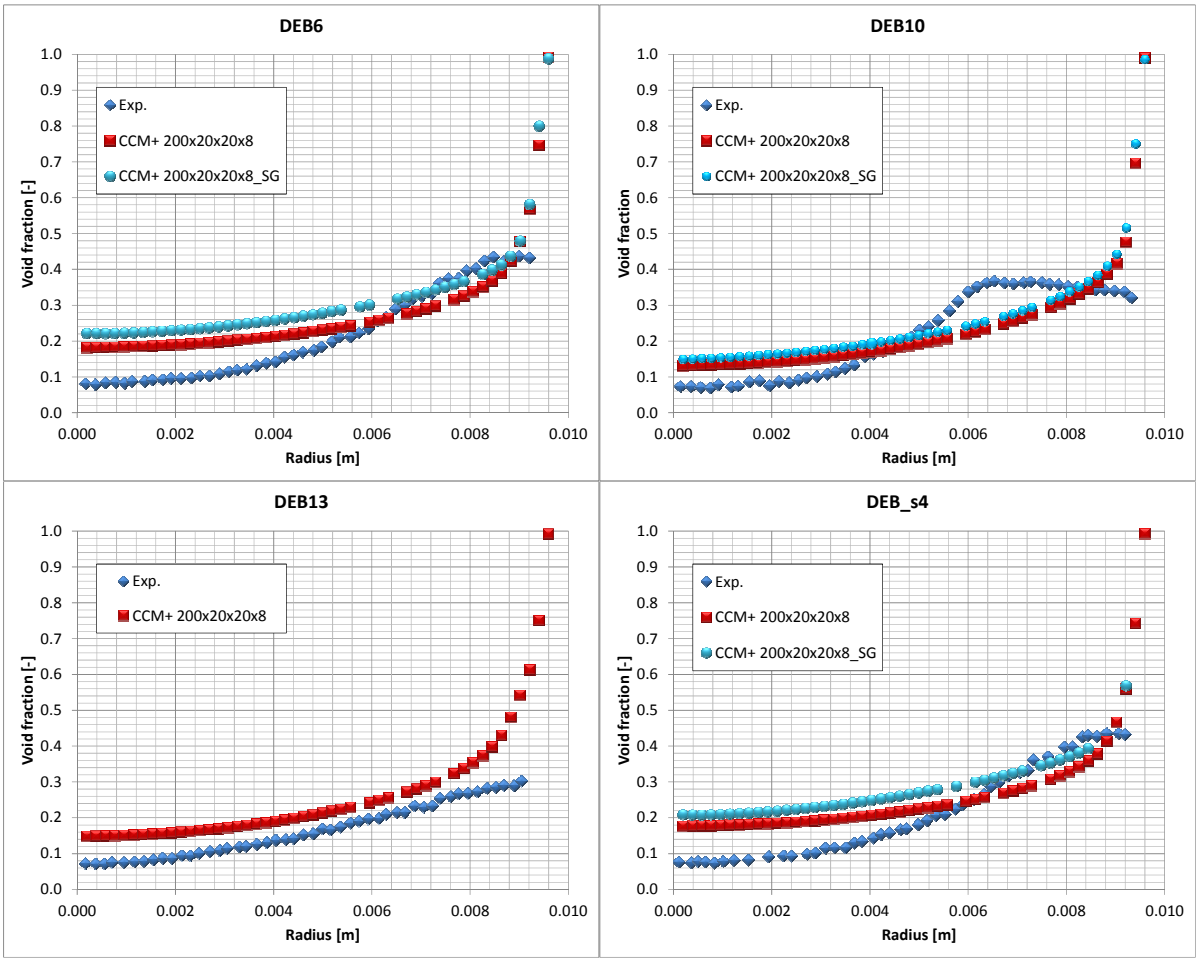

Figure 24 Comparison between computed and experimental void fraction radial distribution.

The radial void fraction profiles obtained with STAR-CCM+ are compared with the experimental data in Figure 24 for selected DEBORA cases characterized by relatively high inlet velocity and heat fluxes. For these cases mesh V7 was employed. Independently on whether S-gamma or Kurul-Podowski formulation is used for the modeling of the bubbles size distribution, the void fraction is systematically overestimated in the center of the cross-section. Consistently with what observed in Figure 21, no significant differences are found between Kurul-Podowski and S-gamma formulations at high cross-section elevations, and thus at the axial measurements location.

For test case DEB10 (see Figure 24) even qualitative agreement is not achieved. For this specific case the Eötvös number is around 4, and therefore still below the threshold of 10 above which an in inversion in the sign of the lift coefficient should be expected. Hence, the shift of the void fraction peak toward the center of the pipe observed in the experimental data cannot be explained by considering the action of the lift force.

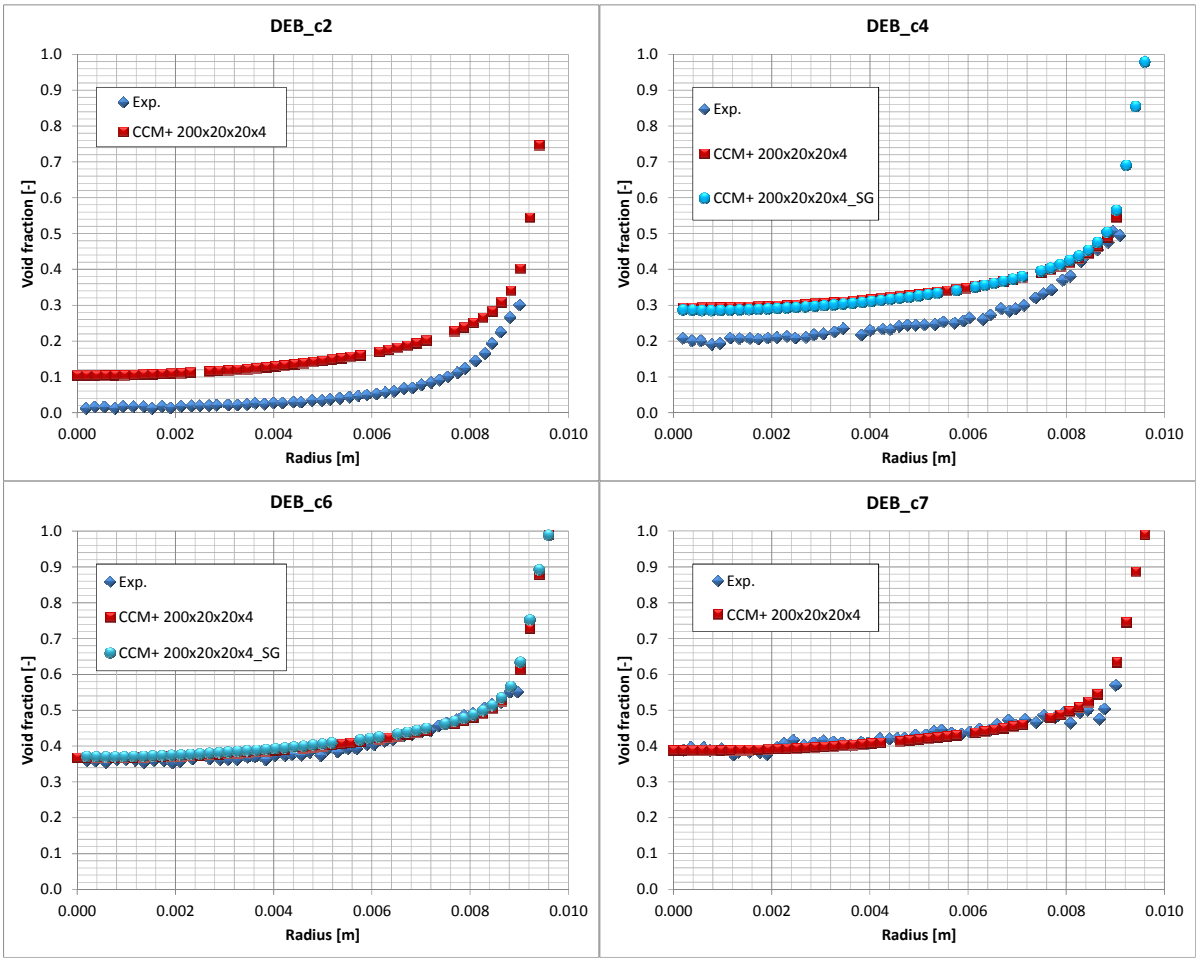

Figure 25 Void fraction distribution for DEB_C2 test case using STAR-CCM+ base model with constant (left) and variable (right) liquid thermodynamics properties.

In Figure 25 the radial void fraction profiles obtained with STAR-CCM+ are compared with the experimental data in Figure 24 for selected DEBORA cases characterized by relatively low inlet velocity, low heat fluxes and high pressure. The overestimation of the void fraction in the center of the cross-section is observed only for cases characterized by higher subcoolings (DEB_C2 and DEB_C4). For lower subcooling excellent agreement between computed and experimental results is found. Again, at the axial measurement location no significant difference is observed when Kurul-Podowski or S-gamma formulations are used.

9 Conclusions

The present report is focused on the validation of the STAR-CD and STAR-CCM+ boiling models against experimental data measured at the PSBT and DEBORA experimental setups. The findings can be summarized as following:

- the cross-section averaged void fraction is systematically overestimated in the low void fraction range, and underestimated in the higher void fraction range. One of the main reasons for this discrepancy lies in the modeling of the bubble size, based on the Kurul and Podowski

formulation. The results in the low void fraction range improve when a more sophisticated model, called S-gamma, is employed for the modeling of the bubble size distribution. The S-gamma formulation is equivalent to a one-group interfacial area transport equation;

- in the high void fraction range the current S-gamma model has practically no effect with respect to the base model. Further improvements of the bubble coalescence and break-up terms are therefore needed at high void fractions;

- the S-gamma model has a considerable effect on the axial void fraction distribution, since at lower axial location smaller bubble sizes are computed. This yields higher condensation rates and therefore lower void fractions than the Kurul-Podowski model.

- the effect of the dependence of the liquid thermodynamic properties on the local temperature should not be neglected.

10 References

[1] Lo, S., Osman, J., 2012. CFD modeling of boiling flow in PSBT 5x5 bundle. *Science and Technology of Nuclear Installations*, Volume 2012, Article ID 795935.

[2] Kurul, N., Podowski, M.Z., 1990. Multidimensional effects in sub-cooled boiling. *Proc. of 9th Heat Transfer Conference*, Jerusalem, 1990.

[3] Yun, B.-J., Splawski, A., Lo, S., Song, C.-H., 2011. Prediction of a subcooled boiling flow with advanced two-phase flow models. *Nuclear Engineering and Design*, in press. Available online since September 2011 (http://dx.doi.org/10.1016/j.nucengdes.2011.08.067).

[4] OECD/NEA Benchmark Based on NUPEC PWR Subchannel and Bundle Tests (PSBT), JNES, November 2010, NEA/NSC/DOC(2010)1.

[5] Star-CD v4.16, Methodology, CD-adapco, 2011.

[6] Drzewiecki T., Asher I., Grunloh T., Petrov V., Fidkowski K., Manera A., and Downar T. 2012. Parameter Sensitivity Study of Boiling and Two-Phase Flow Models in CFD. Selected for publication in *Journal of Computational Multiphase Flows* (special NURETH-14 issue).

[7] Hibiki, T., Ishii, M., Xiao, Z., 2001. Axial interfacial area transport of vertical bubbly flows. *International Journal of Heat and Mass Transfer*, **44**, 1869–1888.

[8] Garnier, J., Manon, E., Cubizolles, G., 2001. Local measurements on flow boiling of refrigerant 12 in a vertical tube. *Multiphase Science and Technology*, **13**, 1–111.

Appendix A - PSBT test cases

Steady State Void Distribution Test Series 1 - Central (Typical) Subchannel S1				
Run No	Pressure	Mass Flux	Power	T(inlet)
	(kg/cm^{2}a)	(10^{6}kg/m^{2}h)	(kW)	(°C)
1.1221	169.1	11.0	49.9	329.7
1.1222	169.1	11.0	50.0	334.7
1.1223	169.1	11.0	49.9	339.7
1.2121	150.1	14.8	79.9	309.5
1.2122	149.9	14.9	80.1	319.7
1.2211	150.1	10.9	90.0	295.4
1.2212	150.1	10.9	90.0	299.4
1.2221	150.1	10.9	69.8	299.4
1.2223	150.1	10.9	69.8	319.6
1.2231	150.2	10.9	60.0	299.3
1.2233	150.2	10.9	59.9	309.6
1.2234	150.1	10.9	60.1	314.6
1.2235	150.1	10.9	59.9	319.6
1.2236	150.0	10.9	60.0	324.7
1.2237	150.3	10.9	60.0	329.6
1.2421	150.2	5.0	59.8	268.9
1.2422	150.1	5.0	60.0	284.1
1.2423	150.3	4.9	59.9	299.3
1.3221	125.0	11.1	59.9	294.4
1.3222	125.1	10.9	60.0	309.5
1.3223	124.9	11.1	60.1	319.7
1.4121	100.1	11.0	69.9	274.1
1.4122	99.8	10.9	69.8	304.5
1.4311	100.4	5.0	79.9	214.2
1.4312	100.2	5.0	79.8	248.9
1.4321	100.5	5.0	59.9	209.3
1.4323	100.5	5.0	59.9	229.2
1.4324	100.1	5.0	60.1	238.9
1.4325	100.3	5.0	59.8	253.8
1.4326	100.1	5.0	60.1	268.8
1.4327	100.1	5.0	59.9	289.0
1.4411	100.4	2.0	19.9	253.7
1.4412	100.3	2.0	20.0	284.0
1.5221	75.5	5.0	49.9	219.2
1.5222	75.0	5.0	50.0	243.9

1.5223	75.6	5.0	49.9	263.8
1.6211	50.4	5.0	79.7	164.1
1.6212	50.4	5.0	79.8	199.3
1.6221	50.5	5.0	50.0	189.2
1.6222	50.0	5.0	49.9	204.2
1.6223	50.5	5.0	49.9	239.0
1.6311	50.6	2.0	20.1	204.1
1.6312	50.6	2.0	20.1	238.9

Steady State Void Distribution Test Series 1 - Central (Thimble) Subchannel S2				
Run No	Pressure	Mass Flux	Power	T(inlet)
	(kg/cm^{2}a)	(10^{6}kg/m^{2}h)	(kW)	(°C)
2.1231	168.9	11.0	37.5	335.0
2.1232	168.8	11.0	37.5	340.0
2.1233	168.8	11.0	37.5	345.0
2.2121	149.5	14.9	60.2	319.9
2.2122	149.5	14.9	60.1	325.1
2.2221	149.9	10.9	60.0	310.4
2.2222	149.9	10.9	60.1	314.9
2.2231	149.9	10.9	52.5	310.3
2.2233	149.9	11.0	52.5	330.6
2.2241	150.0	10.9	45.1	304.3
2.2243	149.9	10.9	45.2	314.5
2.2244	149.9	10.9	45.0	320.0
2.2245	149.9	10.9	45.0	325.5
2.2246	150.0	11.0	45.0	329.8
2.2247	150.0	11.0	45.1	334.8
2.2441	150.4	5.0	45.1	289.8
2.2442	150.4	5.0	45.1	304.8
2.2443	150.4	5.0	45.1	320.1
2.3231	125.2	10.9	45.0	304.6
2.3232	125.1	10.9	45.1	309.8
2.3233	125.0	10.9	45.1	319.9
2.4231	100.3	11.0	52.7	279.3
2.4232	100.2	10.9	52.7	299.6
2.4421	100.4	5.0	60.1	244.0
2.4422	100.5	5.0	60.1	279.2
2.4441	100.5	5.0	45.0	234.1
2.4443	100.5	5.0	45.2	253.9
2.4444	100.6	5.0	45.1	263.9

2.4445	100.5	5.0	45.0	274.0
2.4446	100.5	5.0	45.1	284.2
2.4447	100.5	5.0	45.2	299.4
2.4551	100.7	1.8	15.0	274.0
2.4552	100.7	1.8	15.1	294.3
2.5431	75.6	5.0	37.7	239.0
2.5432	75.7	5.0	37.5	263.9
2.5433	75.6	5.0	37.5	279.2
2.6411	50.5	5.0	60.1	194.2
2.6412	50.5	5.0	60.1	229.2
2.6431	50.6	5.0	37.5	209.2
2.6432	50.6	5.0	37.5	224.2
2.6433	50.5	5.0	37.6	253.9
2.6541	50.7	1.8	15.1	224.1
2.6542	50.7	1.8	15.2	253.7

Steady State Void Distribution Test Series 1 - Side Subchannel S3				
Run No	Pressure	Mass Flux	Power	T(inlet)
	(kg/cm^{2}a)	(10^{6}kg/m^{2}h)	(kW)	(°C)
3.2231	149.9	10.9	40.4	309.4
3.2232	149.9	10.9	40.5	314.5
3.2251	150.0	10.9	30.0	304.3
3.2253	149.9	10.9	30.0	314.4
3.2254	149.9	10.9	30.1	319.5
3.2255	150.0	10.9	30.2	324.5
3.2256	150.0	10.9	30.1	329.6
3.2257	150.0	11.0	30.2	334.5
3.2451	150.3	5.0	30.2	283.8
3.2452	150.5	4.9	30.2	299.0
3.2453	150.3	4.9	30.2	314.3
3.4451	100.5	5.0	30.2	228.9
3.4453	100.5	5.0	30.3	248.8
3.4454	100.4	5.0	30.1	258.6
3.4455	100.6	5.0	30.3	268.8
3.4456	100.6	5.0	30.2	283.7
3.4457	100.6	4.9	30.2	299.0
3.6431	50.4	5.0	40.2	189.0
3.6432	50.4	5.0	40.1	223.9
3.6461	50.6	5.0	25.2	203.9

Steady State Void Distribution Test Series 1 - Corner Subchannel S4				
Run No	Pressure	Mass Flux	Power	T(inlet)
	(kg/cm^{2}a)	(10^{6}kg/m^{2}h)	(kW)	(°C)
4.2231	149.9	11.1	20.3	314.3
4.2232	149.9	11.1	20.3	319.3
4.2251	149.9	11.1	15.2	310.3
4.2253	150.0	11.1	15.1	318.4
4.2254	150.0	11.1	15.2	322.4
4.2255	150.0	11.1	15.2	326.5
4.2256	150.0	11.1	15.1	330.5
4.2257	149.9	11.1	15.1	334.5
4.2451	150.4	5.0	15.2	294.0
4.2452	150.4	5.0	15.2	309.2
4.2453	150.4	5.0	15.2	324.3
4.4451	100.6	5.1	15.2	238.8
4.4453	100.5	5.1	15.2	258.6
4.4454	100.5	5.0	15.1	268.7
4.4455	100.5	5.0	15.2	278.8
4.4456	100.5	5.0	15.2	289.0
4.4457	100.5	5.0	15.2	299.1
4.6431	50.6	5.0	20.2	204.1
4.6432	50.5	5.1	20.3	238.8
4.6461	50.6	5.0	12.5	214.0

Appendix B - DEBORA test cases

Case	Pressure, (bar)	Heat flux, (m/s)	V(inlet), (m/s)	T(inlet), (K)	Tsat, (K)
DEB5	26.15	73890	1.74	341.67	359.881
DEB6	26.15	73890	1.76	343.68	359.881
DEB10	14.59	76.24	1.59	308.06	331.218
DEB13	26.17	109420	2.63	342.35	359.921
S1	14.59	73161	1.56	301.67	331.218
S2	14.59	72054	1.57	304.3	331.218
S3	26.15	73151	1.71	335.88	359.881
S4	26.15	72722	1.76	343.68	359.881
CASE1	30.06	58260	0.83	326.12	367.356
CASE2	30.06	58260	0.84	331.54	367.356
CASE3	30.06	58260	0.85	336.58	367.356
CASE4	30.08	58260	0.88	341.04	367.392
CASE5	30.07	58260	0.88	343.29	367.374
CASE6	30.07	58260	0.90	345.8	367.374
CASE7	30.06	58260	0.89	346.85	367.356